









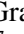






Dust mineralogy and variability of the inner PDS 70 disk

Insights from JWST/MIRI MRS and Spitzer IRS observations

Hyerin Jang ¹, Rens Waters ^{1,2}, Till Kaeufer ^{2,3,4,5}, Akemi Tamanai⁶, Giulia Perotti ⁷, Valentin Christiaens ^{8,9}, Inga Kamp ⁴, Thomas Henning ⁷, Michiel Min², Aditya M. Arabhavi ⁴, David Barrado ¹⁰, Ewine F. van Dishoeck ^{11,12}, Danny Gasman ⁸, Sierra L. Grant ¹², Manuel Güdel ^{13,14}, Pierre-Olivier Lagage¹⁵, Fred Lahuis¹⁶, Kamber Schwarz ⁷, Benoît Tabone¹⁷, and Milou Temmink ¹¹

(Affiliations can be found after the references)

August 30, 2024

ABSTRACT

Context. The inner disk of the young star PDS 70 may be a site of rocky planet formation, with two giant planets detected further out. Recently, JWST/MIRI MRS observations have revealed the presence of warm water vapour in the inner disk. Solids in the inner disk may inform us about the origin of this inner disk water and nature of the dust in the rocky planet-forming regions of the disk.

Aims. We aim to constrain the chemical composition, lattice structure, and grain sizes of small silicate grains in the inner disk of PDS 70, observed both in JWST/MIRI MRS and Spitzer IRS.

Methods. We use a dust fitting model, called DuCK, based on a two-layer disk model considering three different sets of dust opacities. We use Gaussian Random Field and Distribution of Hollow Spheres models to obtain two sets of dust opacities using the optical constants of cosmic dust analogues derived from laboratory-based measurements. These sets take into account the grain sizes as well as their shapes. The third set of opacities is obtained from the experimentally measured transmission spectra from aerosol spectroscopy. We use stoichiometric amorphous silicates, forsterite, and enstatite in our analysis. We also study the iron content of crystalline olivine using the resonance at 23–24 μm and test the presence of fayalite. Both iron-rich and magnesium-rich amorphous silicate dust species are also employed to fit the observed spectra.

Results. The Gaussian Random Field opacity set agrees well with the observed spectrum, better than the other two opacity sets. In both MIRI and Spitzer spectra, amorphous silicates are the dominant dust species. Crystalline silicates are dominated by iron-poor olivine. The 23–24 μm olivine band peaks at 23.44 μm for the MIRI spectrum and 23.47 μm for the Spitzer spectrum, representing around or less than 10 % of iron content in the crystalline silicate. In all of models, we do not find strong evidence for enstatite. Moreover, the silicate band in the MIRI spectrum indicates larger grain sizes (a few microns up to 5 μm) than the Spitzer spectrum (0.1 to 1 μm), indicating a time-variable small grain reservoir.

Conclusions. The inner PDS 70 disk is dominated by a variable reservoir of warm ($T \sim 350\text{--}500\text{ K}$) amorphous silicates, with $\sim 15\%$ of forsterite in mass fraction. The 10 μm and 18 μm amorphous silicate bands are very prominent, indicating that most emission originates from optically thin dust. We suggest that the small grains detected in the PDS 70 inner disk are likely transported inward from the outer disk as a result of filtration by the pressure bump associated with the gap and fragmentation into smaller sizes at the ice line. Collisions among larger parent bodies may also contribute to the small grain reservoir in the inner disk, but these parent bodies must be enstatite-poor. In addition, the variation between MIRI and Spitzer data can be explained by a combination of grain growth over 15 years and a dynamical inner disk where opacity changes occur resulting from the highly variable hot ($T \sim 1000\text{ K}$) innermost dust reservoir.

Key words. methods: data analysis – methods: observational – protoplanetary disks – infrared: planetary systems

1. Introduction

All young solar-type stars are surrounded by a gas-rich and dusty disk in which planets form, and the dust constitutes the fundamental building material for rocky planets in the inner disk (Raymond & Morbidelli 2022). Thus, a better understanding of dust properties in the inner disk is crucial to reveal the evolutionary process of rocky planets which may lead to the development of habitable worlds. At wavelengths shorter than near infrared, observing the dust within a protoplanetary disk is challenging due to the intense flux from the central star. However, at mid-infrared wavelengths, warm dust grains in the inner disk are the main contributors of emission spectra.

PDS 70 is characterized as a K7 spectral type star, and its disk contains a highly dust-depleted gap between the inner and outer disk with a $\sim 54\text{ au}$ separation (Hashimoto et al. 2015, 2012; Long et al. 2018; Keppler et al. 2018). Analysis of continuum observations from the Atacama Large Millimeter/submillimeter Array (ALMA) constrains the dust mass of

the inner disk ($< 18\text{ au}$) to $0.08\text{--}0.36\text{ M}_{\oplus}$ (Benisty et al. 2021). Within the gap, two giant protoplanets, PDS 70b and PDS 70c, have been detected (Keppler et al. 2018; Müller et al. 2018; Wagner et al. 2018; Haffert et al. 2019; Isella et al. 2019), and there is strong evidence that these planets are still accreting (Aoyama & Ikoma 2019; Haffert et al. 2019; Thanathibodee et al. 2019; Hashimoto et al. 2020; Zhou et al. 2021; Campbell-White et al. 2023). Recently, James Webb Space Telescope (JWST; Rigby et al. 2023) Near Infrared Camera Instrument and Near Infrared Imager and Slitless Spectrograph observations of the PDS 70 disk have detected the two protoplanets, with a circumplanetary disk around PDS 70c, and a potential third protoplanet at around 13.5 au distance from the star (Mesa et al. 2019; Christiaens et al. 2024b; Blakely et al. 2024). The PDS 70 system has also been observed with the JWST Mid-Infrared Instrument (MIRI; Rieke et al. 2015; Wright et al. 2015, 2023) by the MIRI mid-Infrared Disk Survey (MINDS; Henning et al. 2024). Perotti et al. (2023) report the detection of warm water vapour ($\sim 600\text{ K}$) in the in-

ner disk. By using a two-layer disk model, the authors define the dust continuum and identify crystalline and amorphous silicate emission bands.

Silicate stands as the predominant material of dust in both the interstellar medium and protoplanetary disks (Dorschner et al. 1995; Colangeli et al. 2003; Henning 2010). Silicates in the interstellar medium are mainly amorphous (Kemper et al. 2004; Chiar & Tielens 2006) whereas the presence of crystalline silicates is confirmed in protoplanetary disks (Bouwman et al. 2001; van Boekel et al. 2004; Forrest et al. 2004; van Boekel et al. 2005; Kessler-Silacci et al. 2005; Apai et al. 2005; Kessler-Silacci et al. 2006; Olofsson et al. 2009; Sargent et al. 2009; Watson et al. 2009; Sicilia-Aguilar et al. 2009; Juhász et al. 2010; Olofsson et al. 2010; Oliveira et al. 2011; Sturm et al. 2013). The formation of crystalline silicates involves either gas phase condensation or thermal annealing of amorphous silicates (Bradley et al. 1983). Therefore, crystalline silicates in disks can trace the thermal history of dust together with amorphous silicates. The dominant dust components are magnesium-iron (Mg-Fe) silicates for both amorphous and crystalline forms. Particularly, crystalline olivine ($\text{Mg}_{2x}\text{Fe}_{2-2x}\text{SiO}_4$ ($0 \leq x \leq 1$)) and crystalline pyroxene ($\text{Mg}_x\text{Fe}_{1-x}\text{SiO}_3$ ($0 \leq x \leq 1$)) have been detected in various astronomical environments. Likewise, amorphous Mg-Fe silicates having the same chemical formula as mentioned above are one of the most abundant components of dust grains. Identifying these dust species in protoplanetary disks is possible through the shapes of their opacities at infrared wavelengths, that reflect the chemical composition, lattice structure, grain size, and shape of dust grains.

Infrared spectroscopy can be used to study the spatial distribution of crystalline silicates, because of the wide wavelength range accessible and the availability of resonances that probe both warm and cold dust (Juhász et al. 2010; Olofsson et al. 2009, 2010; Sturm et al. 2013; Espaillat et al. 2011). For instance, Juhász et al. (2010) measured the mass fraction of forsterite (crystalline Mg_2SiO_4) and enstatite (crystalline MgSiO_3) at two different wavelength ranges for Herbig Ae/Be stars observed with the Spitzer Space Telescope (Spitzer) InfraRed Spectrograph (IRS): in the wavelength range of 5-17 and 17-35 μm , representing inner and outer disk, respectively. From the comparison, they found that forsterite is more abundant than enstatite in the outer disk, and vice versa for the inner disk. Olofsson et al. (2009) and Olofsson et al. (2010) investigated crystalline silicates in Spitzer IRS spectra of protoplanetary disks around a large sample of T-Tauri stars. In both warm (emitting at $\lambda \sim 10 \mu\text{m}$) and cold (emitting at $\lambda > 20 \mu\text{m}$) regions in the disks, crystalline silicate bands of forsterite, enstatite, and diopside ($\text{CaMgSi}_2\text{O}_6$) were detected. The crystallinity of the inner and outer disk was found to be roughly similar at average values of 16 and 19 %, respectively, however with some disks showing a higher outer disk crystallinity compared to the inner disk. Moreover, Sturm et al. (2013) analyzed the 69 μm forsterite band in Herbig Ae/Be and T-Tauri disks using Herschel. Sources that show the 69 μm band are well fitted with Mg-rich forsterite, with an upper limit to the iron content of 2-4 %; the forsterite was found to be at 100-200 K, i.e. far out in the disk beyond ~ 10 au.

The distinctive shapes of band features in opacities of silicate dust species enable us to identify specific silicate species within the disk. Dust opacities can be calculated for a range of grain sizes by adopting a grain shape model. One such theoretical model is the Distribution of Hollow Sphere (DHS; Min et al. 2005). DHS provides a distribution for the fraction of empty space within a hollow sphere and measures their opacity. Another theoretical model, the Gaussian Random Field (GRF; Min

et al. 2007), generates individual grain surface roughness based on a Gaussian random field and calculates the average opacity over a range of the individual shapes of the porous GRF particle. Min et al. (2007) employed the Discrete Dipole Approximation (DDA) to compute the opacity of the porous GRF particles and selected particles containing 2000-3500 dipoles. For more details on this method, we refer to Min et al. (2006, 2007).

Dust opacities can also be directly measured from aerosol particles. This method has the advantage that it avoids theoretical assumptions about grain shape and size (Tamanai et al. 2006, 2009). In the aerosol experiments, micron-sized aerosol of dust species are measured with a Fourier transformation infrared spectrometer under a condition close to vacuum. This setup ensures that the grain shapes and their environment could closely mimic those of dust in the universe. Given that the shapes of opacity curves are influenced by measurement methods, it becomes crucial to use appropriate opacity curves for accurate dust fitting.

In this study, we use these dust opacities to analyze the inner-disk dust of the PDS 70 disk observed with JWST/MIRI Medium Resolution Spectrometer (MRS; Argyriou et al. 2023) and Spitzer IRS. We focus on the quantitative analysis of silicate dust bands within the PDS 70 disk. Specifically, we aim to reveal dust species, grain sizes, and their mass abundances. In Sect. 2 we introduce the JWST/MIRI MRS observations and the data reduction, and we present the Spitzer IRS observations. In Sect. 3, we describe the dust fitting model, DuCK, that we use to analyze dust bands in the spectrum. The results from fitting with different sets of opacities are shown in Sect. 4, and we also investigated fraction of iron in silicate dust in Sect. 5. Section 6 shows fitting results of the Spitzer spectrum for comparison to the MIRI spectrum. We discuss our fitting results, variability between the MIRI and Spitzer spectra, and origin of the inner-disk small grains in Sect. 7. Conclusions are summarized in Sect. 8.

2. Spitzer IRS and JWST/MIRI MRS observations and data reduction

The PDS 70 disk has been observed with both Spitzer IRS and JWST/MIRI MRS with these observations being 15 years apart. With Spitzer IRS, the observation was conducted in low-resolution ($R \sim 60-100$) in 2007 as a part of program 40679 (PI: G. Rieke), and we use its reduced data, introduced in Perotti et al. (2023). These spectra are shown together with the JWST/MIRI MRS observation in Fig. 1. The Spitzer spectrum shows a spike at 14 μm due to imprecise stitching of the data, but its peak and shape do not match with any of dust bands we have. Thus, the spike does not affect to the dust fitting process.

2.1. JWST/MIRI MRS

PDS 70 was observed on August 1, 2022 with the MRS of the MIRI instrument, having spectral resolving power $R \sim 1,600 - 3,400$. This observation was part of the Guaranteed Time Observation (GTO) program 1282 (PI: Th.Henning), called MINDS (Henning et al. 2024). The observational strategy and data reduction are already explained in Perotti et al. (2023), so we summarize the overall process and slight differences in the process.

In short, the observed data were reduced using the MINDS pipeline (v1.0.0; Christiaens et al. 2024a), a hybrid pipeline leveraging on the one hand the JWST Science Calibration pipeline (version 1.12.5; Bushouse et al. 2023) along with the Calibration Reference Data System (CRDS) context

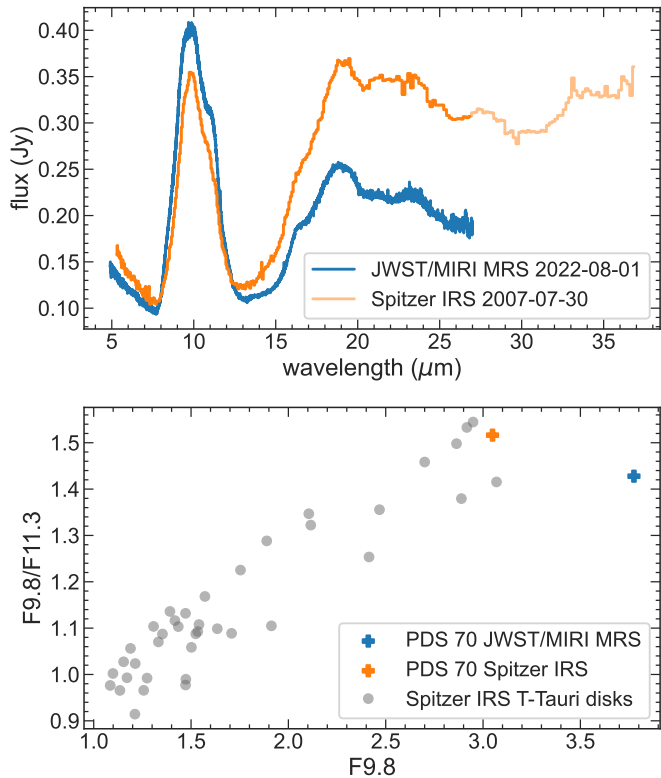


Fig. 1: The MIRI and Spitzer spectra of PDS 70 and their shapes of $10\ \mu\text{m}$ silicate bands. *Upper*: MIRI spectrum is in blue, and Spitzer spectrum is in orange. Light orange shows full wavelength range of the Spitzer spectrum. Around $10\ \mu\text{m}$, the MIRI spectrum has a higher flux and broader silicate band while the Spitzer spectrum shows higher flux levels beyond $12\ \mu\text{m}$. *Lower*: Band strength at $9.8\ \mu\text{m}$ and the shape of $10\ \mu\text{m}$ silicate band. Gray dots are disks in CASSIS database with low resolution spectra. Blue cross is the MIRI spectrum while orange cross is the Spitzer spectrum.

jwst_1118.pmap, and on the other hand the Vortex Image Processing (VIP; Gomez Gonzalez et al. 2017; Christiaens et al. 2023) package for tasks such as bad pixel correction, background subtraction, and source centroid finding.

In Detector1 and Spec2 stages of the pipeline, the uncalibrated raw data and rate files were processed with default parameters, respectively. Apart from the outlier detection step of Spec3, bad pixels were also identified and corrected through iterative sigma-filtering and a two-dimensional Gaussian kernel with the VIP package before Spec3. In Spec3, a Gaussian fit on the weighted average image of each band was used to determine the centroid for aperture photometry. A 2-FWHM (full width at half maximum) aperture was considered for spectrum extraction, and the background level was estimated from a surrounding annulus.

2.2. Characterization of the $10\ \mu\text{m}$ silicate band

Around $10\ \mu\text{m}$, MIRI spectrum shows a higher and broader flux emission compared to Spitzer while the fluxes are lower in the MIRI spectrum beyond $12\ \mu\text{m}$ as shown in Fig. 1. Calibration uncertainty of the MIRI spectrum is ruled out for any differences greater than 5 % (Perotti et al. 2023). The difference is $\sim 10\ \%$

below $12\ \mu\text{m}$ and $\sim 40\ \%$ above $12\ \mu\text{m}$. The reported spectrophotometric accuracy is 2–10 % for Spitzer IRS (Furlan et al. 2006; Watson et al. 2009) and $5.6\% \pm 0.7\%$ for JWST/MIRI MRS (Argyriou et al. 2023). The JWST Science Calibration pipeline version 1.12.5 that we used takes into account the time-dependent sensitivity of the MIRI MRS. This variability in the PDS 70 disk is not only found at mid-infrared wavelengths but also at shorter wavelength ranges (Gaidos et al. 2024). At the longer wavelengths beyond $12\ \mu\text{m}$, we can also see clear forsterite bands at 16 and $19\ \mu\text{m}$ in MIRI and Spitzer spectra. However, the presence of the $23\ \mu\text{m}$ band is not obvious in the Spitzer spectrum, but we identify it in the MIRI spectrum.

The strength of the $10\ \mu\text{m}$ silicate band in the PDS 70 disk is unusually strong for a T-Tauri disk. To illustrate this, we measured the band strengths and shapes of the $10\ \mu\text{m}$ silicate band for both MIRI and Spitzer spectra (following van Boekel et al. 2003 and Olofsson et al. 2009) and compared with a sample of T-Tauri disks and pre-transitional disks from the Spitzer CASSIS database (Lebouteiller et al. 2011) in the lower panel of Fig. 1. The band strength at $9.8\ \mu\text{m}$ ($F_{9.8}$) is measured as

$$F_{9.8} = 1 + (f_{9.8\ \mu\text{m,cs}} / \langle f_c \rangle), \quad (1)$$

where $f_{9.8\ \mu\text{m,cs}}$ is the linear continuum subtracted flux at $9.8\ \mu\text{m}$, and $\langle f_c \rangle$ is the mean of the linear continuum. The linear continuum is drawn from $7.5\ \mu\text{m}$ to $12.7\ \mu\text{m}$. We also measured the ratio of band strengths at $9.8\ \mu\text{m}$ and $11.3\ \mu\text{m}$ ($F_{9.8}/F_{11.3}$), representing the shapes of $10\ \mu\text{m}$ silicate band. We can see that the PDS 70 disk has very strong $9.8\ \mu\text{m}$ strength and convex shape, representing dominant amorphous small grain population in the disk (van Boekel et al. 2003; Olofsson et al. 2009).

Disks with larger grains move to the lower left of the diagram in the lower panel of Fig. 1 (van Boekel et al. 2003; Furlan et al. 2006). Clearly, the difference between the MIRI and Spitzer spectra does not follow this trend. The MIRI spectrum has smaller $F_{9.8}/F_{11.3}$ value, so we expect to see larger grains in the MIRI spectrum compared to Spitzer data (smaller $F_{9.8}$ value). However, the $F_{9.8}$ value in the MIRI spectrum is larger than in the Spitzer spectrum, indicating the presence of smaller grains. Another factor affecting the $F_{9.8}/F_{11.3}$ value is crystallinity, so the small grains might be highly crystalline in the PDS 70 disk. This behavior still does not align with the overall trend observed in other T-Tauri disks as shown in Fig. 1. This, combined with the unusually strong silicate band, indicates that the grain population probed by these spectra may be different from that seen in other disks.

3. Dust fitting method

We used the Dust Continuum Kit (DuCK; Kaeufer et al. (2024)) to identify dust species in the PDS 70 disk. DuCK is a part of Dust Continuum Kit with Line emission from Gas (DuCKLinG), which is able to simultaneously account for the gas and dust contributions to mid-infrared spectra. However, we only use the dust continuum part, which is identical in its setup to the two-layer disk model introduced by Juhász et al. (2009, 2010). The model and fitting procedure are described in Sect. 3.1. Section 3.2 describes the modeled stellar photospheric spectrum for the PDS 70, the reduced MIRI spectrum onto a wavelength grid of lower and constant spectral resolving power, opacities of the dust from different grain shape models and laboratory measurement, and the temperature setup in DuCK model.

3.1. DuCK model

DuCK is a retrieval model to fit the dust continuum of a protoplanetary disk spectrum (Kaeufer et al. 2024). DuCK consists of the star, inner rim, optically thin disk surface, and optically thick midplane, and superposes these components (Juhász et al. 2009, 2010). Thus, the modeled flux density is

$$F_\nu = F_\nu^{\text{star}} + F_\nu^{\text{rim}} + F_\nu^{\text{mid}} + F_\nu^{\text{sur}}, \quad (2)$$

where F_ν^{star} , F_ν^{rim} , F_ν^{mid} , and F_ν^{sur} are the fluxes of the star, the inner rim, the midplane, and the disk surface, respectively. The flux of the inner rim (F_ν^{rim}) describes the emission coming from the inner edge of the disk and is described by the Planck function at the temperature of the inner rim (T_{rim}) and a scaling factor (sc_{rim}). The scaling factor represents the size of the emission area of the inner rim. The midplane flux summarizes the optically thick dust emission in a disk, that can be approximated by a radial temperature powerlaw with the exponent (q_{mid}) between the minimum ($T_{\text{mid,min}}$) and maximum temperatures ($T_{\text{mid,max}}$) and another scaling factor (sc_{mid}). The last component contributing to the model flux is the disk surface, which accounts for the optically thin dust emission from a disk. The temperature is following, analogous to the midplane, a radial temperature powerlaw with the exponent (q_{sur}) between the minimum ($T_{\text{sur,min}}$) and maximum temperatures ($T_{\text{sur,max}}$).

The fit quality of a model is determined by the likelihood using the model fluxes and the observational fluxes with their uncertainties for all spectral points (see Eq. 14 in Kaeufer et al. 2024). Moreover, the temperature parameters (T_{rim} , $T_{\text{mid,min}}$, $T_{\text{mid,max}}$, T_{sur} , and q_{mid}) are sampled in a Bayesian way using MultiNest (Feroz & Hobson 2008; Feroz et al. 2009, 2019) while the scale parameters and dust abundances are determined by using a non-negative least square fitting with SciPy (Virtanen et al. 2020). Linear fitting during the Bayesian analysis decreases the number of parameters sampled by MultiNest and, therefore, decreases the computational cost of the fitting. Kaeufer et al. (2024) shows that the retrieved results are largely consistent with a full Bayesian analysis of all parameters.

3.2. Fitting model setup

The emission of the star (F_ν^{star}) is described by a modeled stellar photospheric spectrum, using PHOENIX code (Baron et al. 2010), of an effective temperature $T_{\text{eff}} = 4,000$ K, surface gravity $\ln(g) = 4.5$, and solar metallicity, used in Perotti et al. (2023). The modeled stellar spectrum was extrapolated ($\propto \lambda^{-2}$) to the mid-infrared wavelengths and was averaged every 15 data points to avoid biased fitting results at short wavelength due to high resolution of the stellar model.

We rebinned the MIRI spectrum ($R \sim 3000$) onto a wavelength grid of constant spectral resolving power ($R \sim 500$). We first generate a wavelength grid that has a constant spectral resolution. From the spectrum, we measured the mean and standard deviation of fluxes within every wavelength grid. Thus, we could find the normal error distribution of the equally weighted spectrum. This method is valid because we do not fit gas and dust emissions together and assume the spectrum is fully due to dust emission. Perotti et al. (2023) only identify H_2O and CO_2 emission lines, and the spectrum is not dominated by these molecular emissions. The typical errorbar of individual spectral points of the MIRI spectrum is reported as 0.2 mJy in Perotti et al. (2023), but we have errorbars as large as 1 – 3 mJy because of the weak gas emission. We note that the fitting results are not sensitive to the value of spectral resolving power whether it is $R \sim 300$ or

700, and $R \sim 500$ is good enough to represent dust bands present in the spectrum.

We use three different sets of opacities to fit the MIRI and Spitzer spectra: Distribution of Hollow Sphere (DHS, Min et al. (2005)), Gaussian Random Field (GRF, Min et al. (2007)), and optical data obtained from laboratory-based aerosol spectroscopy (hereafter Aerosol) (Tamanai et al. 2006, 2009). The optical constants, which are derived from experimentally measured reflectance spectra by using the Kramers–Kronig relations (e.g., Jäger et al. 1998), are applied for both GRF and DHS models and listed in Table 1. These optical constants are converted to opacities using two grain shape models of irregularly shaped dust grains, GRF and DHS. On the other hand, the extinction spectra can be obtained via Aerosol spectroscopy. Particulates are suspended and retained in nitrogen (N_2) gas flow during the in-situ measurements. Since the refractive index of the gas is comparable to that of vacuum, these experimentally obtained extinction spectra are not affected by the medium at all.

Table 1 shows the optical constants of amorphous and crystalline silicates as well as amorphous SiO_2 for GRF and DHS calculations. We select two types of crystalline silicates: forsterite and enstatite, together with stoichiometric amorphous Mg_2SiO_4 , Mg_2SiO_4 , and SiO_2 . In DHS, the inner volume fraction of hollow sphere (f_{max}) was set to be 0.99 for crystalline dust and 0.7 for amorphous dust (Min et al. 2005, 2007). All dust grains have sizes of 0.1, 1, 2, 3, 4, 5 μm . Grain sizes greater than 5 μm are not considered in DuCK model because the band strength becomes very weak already for 5 μm -sized grains. We note that DuCK does not use grain size distributions, so the absence of intermediate grain sizes between the detected smallest and largest sizes in results does not imply that these sizes do not exist in the disk. Rather, the best-fit DuCK result is consistent with a spectrum, therefore no further grain sizes are necessary. In Aerosol, we pick out the individual particle size around 1 μm for each measurement; however, the extinction spectra contain the agglomerates composed of micron-sized particles as well. Absorption efficiencies of amorphous and crystalline Mg_2SiO_4 in DHS and GRF together with the Aerosol spectrum are shown in Fig. 2. We note that Aerosol spectra are experimentally measured non-quantitative absorbance, so the intensity varies depending the particle concentration. Therefore, we normalized the aerosol spectra using the right y-axis in Fig. 2. Moreover, the DHS and GRF opacities are converted to absorption efficiencies by multiplying them by $4/3\pi a \rho \kappa_{\text{abs}}$, where a is the grain size, ρ is the material density, and κ_{abs} is the DHS and GRF opacities. In the case of amorphous Mg_2SiO_4 (upper panel), overall band profiles of absorption efficiencies calculated by the GRF and DHS are well consistent with the Aerosol. By contrast, absorption peaks of crystalline Mg_2SiO_4 calculated by the DHS undergo a clear redshift at longer wavelengths ($\lambda > 15 \mu\text{m}$) compared to the GRF and Aerosol spectra (bottom panel). First, we focus on Mg-rich silicates to fit the spectrum, but we also try to include Fe-rich silicates, such as fayalite (crystalline Fe_2SiO_4) and amorphous MgFeSiO_4 and $\text{MgFeSi}_2\text{O}_6$ in Sect. 5.2.

In DuCK, we set the priors for temperatures of the inner rim, the disk surface, and the midplane as $T_{\text{rim}} = [1000, 1500]$, $T_{\text{sur}} = [150, 700]$, $T_{\text{mid,min}} = [10, 1000]$, $T_{\text{mid,max}} = [10, 1000]$. The exponent for the temperature gradient of the midplane is $q_{\text{mid,min}} = [-1.5, -0.1]$. We adjusted the priors to be large enough to cover full posterior probability distributions within a reasonable temperature range for a protoplanetary disk. The posterior probability distributions for the best model in this study (discussed in the next section) is shown in Fig. B.1. In addition,

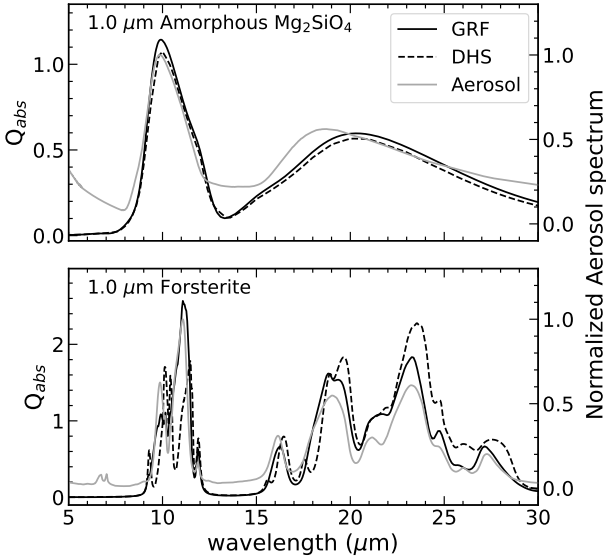


Fig. 2: Comparison among absorption efficiencies for amorphous Mg_2SiO_4 (upper panel) and forsterite (lower panel). GRF (black solid line) and DHS (dashed line) are plotted for Q_{abs} on the left y-axis, and Aerosol spectra (gray solid line) are normalized on the right y-axis.

DuCK allows for measuring disk surface flux with a single temperature instead of the temperature gradient.

4. Dust fitting with different opacities

We first conducted a fitting process using a temperature gradient for the disk surface, which results in $T_{\text{sur,min}} = 460$ K and $T_{\text{sur,max}} = 490$ K. Due to the small temperature range, fitting can be performed with a single temperature for the disk surface. Importantly, the results remain consistent with the single disk surface temperature. Thus, we proceed to fit the PDS 70 spectrum using a single temperature for the disk surface. Mass fractions of each species and grain sizes of the fitting with GRF, DHS, and Aerosol are summarized in Table A.1, and temperatures of the inner rim, the disk surface, and the midplane are plotted in Fig. 3. Fitting results are also shown in Fig. 4, Fig. A.1, and Fig. A.2.

Model GRF: Using GRF opacities, the dominant dust species is amorphous silicates contributing ~ 79 % of the surface layer dust mass, with crystalline silicate at ~ 20 %. We find no evidence for enstatite and amorphous SiO_2 . Most silicate species are a few microns in size while amorphous MgSiO_3 shows significant mass fraction of $0.1 \mu\text{m}$ grains with ~ 33 %. The inner rim temperature is ~ 1400 K, the disk surface is ~ 500 K, and the midplane has temperature gradient from 25 K to 200 K as shown in Fig. 3. The mean residual of this fit is around 1.3 %, and the overall residual is shown in Fig. 4. The largest residual appears at $8 \mu\text{m}$ because the shapes of GRF dust opacities do not perfectly match at the start of the slope of $10 \mu\text{m}$ silicate band. Other than the spike, the overall quality of the fit is in good agreement with the MIRI spectrum.

Model DHS: Using DHS opacities, amorphous silicate dominates the spectrum, even more than in Model GRF at ~ 94 % of the optically thin dust mass fraction, with forsterite at ~ 5 %, i.e. a significantly lower crystallinity compared to Model GRF. $0.1 \mu\text{m}$ -sized amorphous MgSiO_3 is still the most dominant dust

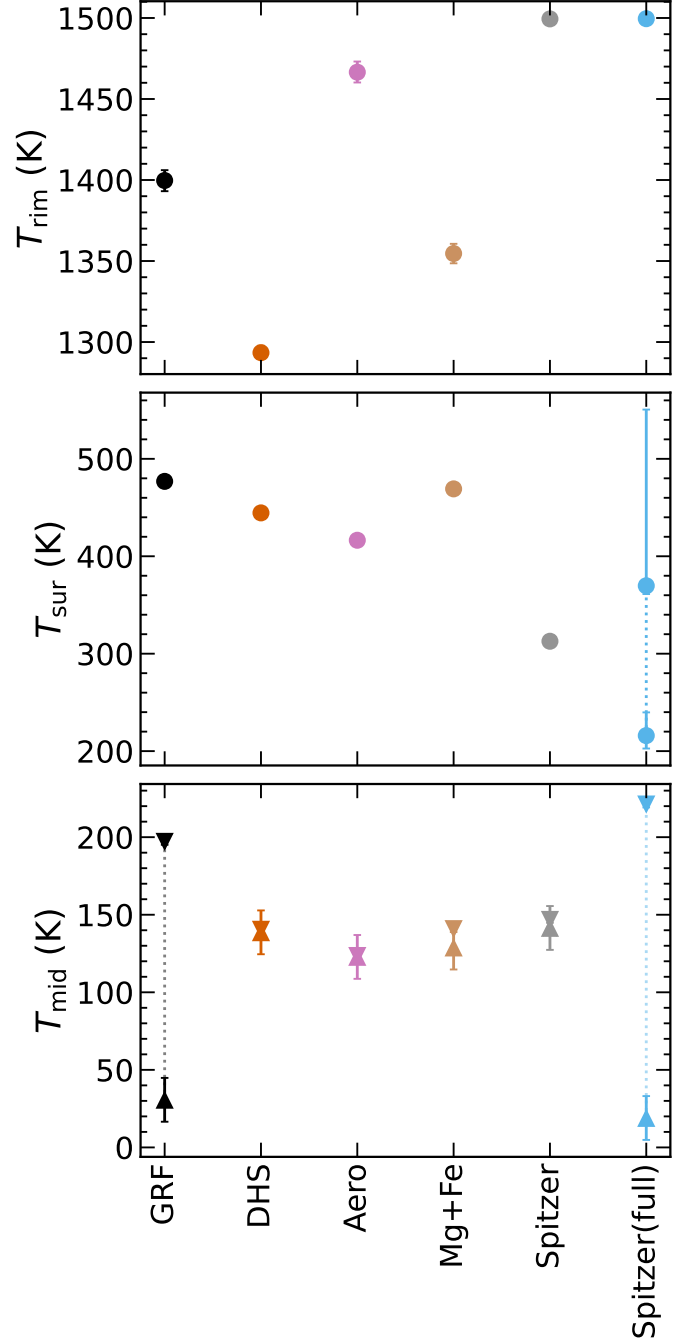


Fig. 3: Temperatures of dust in the inner rim (top), disk surface (middle), and midplane (bottom) of dust fitting models in Table A.1. For Spitzer(full), the dotted line in the temperature of the disk surface indicates the temperature gradient across the disk surface; the other models assume a single temperature.

grain species, and $0.1 \mu\text{m}$ -sized forsterite is found at a mass fraction of ~ 3 %. Unlike Model GRF, grain sizes larger than $2 \mu\text{m}$ are not found in this model. Enstatite and amorphous SiO_2 are still not detected. The inner rim temperature is around 1300 K, which is lower than Model GRF. The disk surface temperature is ~ 450 K, similar to Model GRF, while the midplane temperature is ~ 140 K, much narrower temperature range as shown in the lower panel of Fig. 3. The mean residual is 1.5 %, as shown in Fig. A.1. Around $20 \mu\text{m}$, the forsterite band of our model is slightly red-shifted and overestimated compared to the MIRI

Table 1: Optical constants used to generate opacities with GRF and DHS.

species	reference
Forsterite	Servoin & Piriou (1973)
Enstatite	Jäger et al. (1998)
Fayalite	Fabian et al. (2001)
Amorphous Mg_2SiO_4	Henning & Stognienko (1996) ¹
Amorphous MgSiO_3	Dorschner et al. (1995)
Amorphous SiO_2	Henning & Mutschke (1997)
Amorphous MgFeSiO_4	Dorschner et al. (1995)
Amorphous $\text{MgFeSi}_2\text{O}_6$	Dorschner et al. (1995)

¹ The optical constant can be found from this website:
https://www2.mpa-hd.mpg.de/homes/semenov/Opacities/RI/new_ri.html

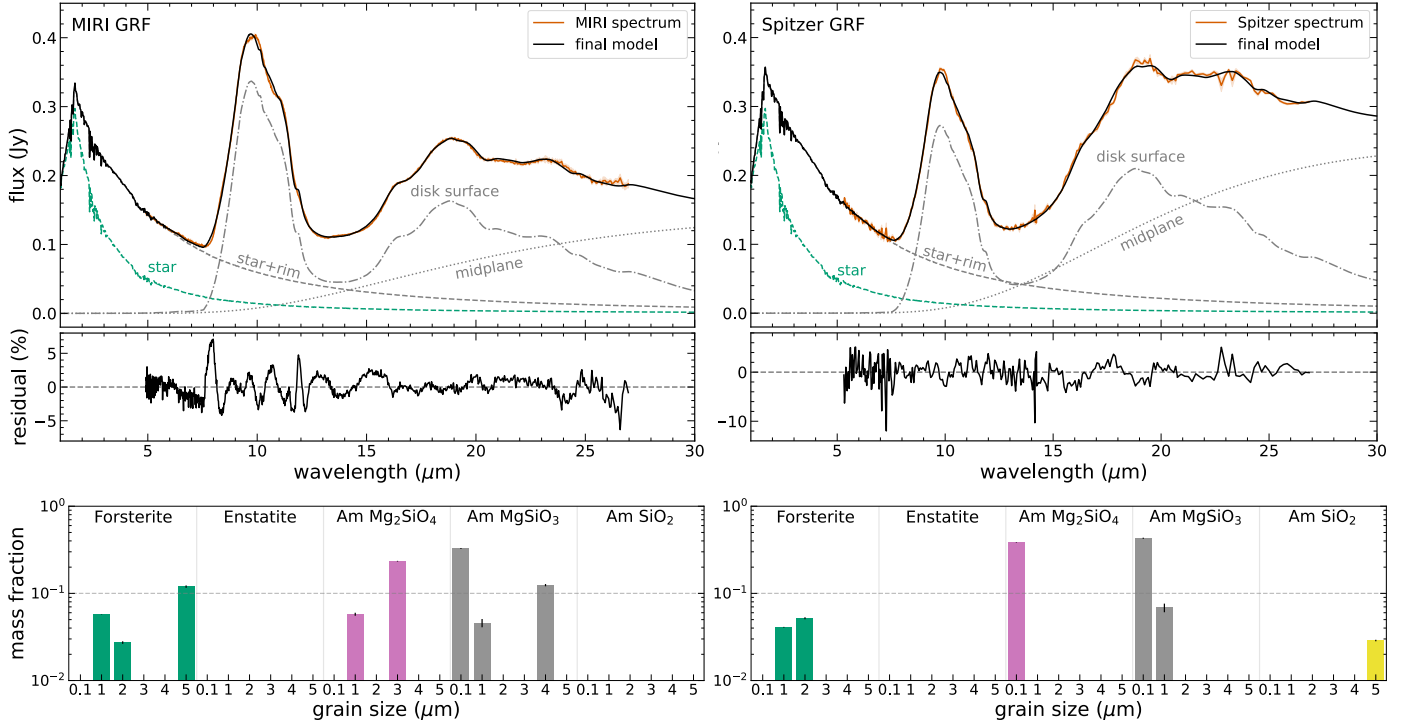


Fig. 4: Fitting with GRF opacity. The modeled spectrum matches well with the MIRI spectrum with the mean residual less than 2 %. Amorphous silicates dominate the dust mass abundance, and 0.1 μm -sized amorphous MgSiO_3 is the most abundant species. Enstatite and amorphous SiO_2 do not show up from the fitting.

spectrum while Model GRF does not show this mismatch. This red-shifted forsterite band on DHS is also seen in opacities of forsterite in Fig. 2, compared to GRF.

Model Aerosol: The overall shape of the fitting aligns with the spectrum as shown in Fig. A.2. Nevertheless, the peak of 10 μm silicate band and 21 μm band are overestimated while the 16 μm band is underestimated. Both shoulders of the 10 μm silicate band are also underestimated or overestimated. As other models with GRF and DHS, amorphous silicates dominate the spectrum with 95 %. However, amorphous Mg_2SiO_4 is the dominant species among amorphous silicates. Unlike Model GRF and DHS, enstatite and amorphous SiO_2 are found with $\sim 2\%$ and $\sim 7\%$, respectively. The inner rim temperature is relatively higher than other models at ~ 1450 K, but the disk surface temperature is slightly lower at ~ 400 K. The midplane temperature is ~ 125 K, similar to Model DHS. We find that the use of Aerosol absorption efficiencies results in fitting residuals that are signifi-

cantly larger than for the other two models. The mean residual is around 3.7 %, and the maximum residual is around 15 % as shown in Fig. A.2. This is expected, because the Aerosol measurements are limited in the range of grain sizes and shapes that are sampled.

We use the logarithm of the Bayes factor to assess the quality of the fits presented above. The bayes factor is defined as the difference between the Nested sampling Global Log-Evidence of models ($\ln(\text{Model})$), denoted as $\ln B_{1,2} = \ln(\text{Model1}) - \ln(\text{Model2})$. The Nested sampling Global Log-Evidence comes as a result of MultiNest. If the bayes factor for Model1 and Model2 ($\ln B_{1,2}$) is smaller than 1, it represents that Model1 has no evidence over Model2 (Trotta 2008). Model DHS and Model Aerosol have negative Nested sampling Global Log-Evidence, while Model GRF is $\ln(\text{Model GRF}) = 937$. Thus, $\ln B_{\text{GRF, DHS}}$ and $\ln B_{\text{GRF, Aerosol}}$ are very negative, and Model GRF is clearly

the preferred model over others. Therefore, we focus mainly on the GRF opacity in the remainder of this study.

Model GRF and Model DHS show the forsterite mass fractions of 20.4% and 4.6%, respectively. In Model GRF, the dominant forsterite mass comes from the largest grains ($5\mu\text{m}$), which contribute the least to the flux compared to the smaller grains. To test the dependence of the crystalline mass fraction on the largest grain size, we fitted the same GRF model but excluded the large forsterite grains in Model GRF $4\mu\text{m}$ (forsterite up to $4\mu\text{m}$) and Model GRF $2\mu\text{m}$ (forsterite up to $2\mu\text{m}$). As the large grains are depleted, the crystalline mass fraction decreases. In Model GRF $4\mu\text{m}$ and Model GRF $2\mu\text{m}$, the mass fractions of the largest grains slightly decrease to $\sim 18\%$ and $\sim 12\%$, respectively. Although we neglect the largest forsterite grains in Model GRF $4\mu\text{m}$ and Model GRF $2\mu\text{m}$, crystallinity remains at the same magnitude, and the largest forsterite is always preferred in those models. Moreover, the mass fractions for each grain size also depend on the grain shape model. Model DHS has no contribution to crystallinity from the large grains because forsterite bands quickly decrease in strength for $1\mu\text{m}$ -sized grains. Thus, the crystallinity in mass fraction may depend on the largest grain size given in the model and grain shape model, but the crystallinity is always greater than 10% based on Model GRF, Model GRF $4\mu\text{m}$, and Model GRF $2\mu\text{m}$.

5. Iron-containing silicates

In the previous section, we used opacities from pure Mg silicates, but iron, being highly refractory, condenses into the solid phase. Iron-containing silicates, another end member of olivine and pyroxene stoichiometry, could exist in the PDS 70 inner disk. Iron-containing silicates have been detected in warm debris disks (Olofsson et al. 2012), and in a small number of gas-rich T-Tauri disks (Olofsson et al. 2010). We explore the iron content in the PDS 70 disk through two methods: measuring the peak of the $23\text{--}24\mu\text{m}$ crystalline silicate band (Sect. 5.1) and dust fitting with Fe-rich silicates (Sect. 5.2). We note that iron may also exist as FeS or metallic iron. While metallic iron contributes opacity, it lacks infrared vibrational resonances, making its direct detection difficult with our method. FeS also has generally weak mid-infrared resonances. Its main band centered at $23.5\mu\text{m}$ is too broad in the region where the $18\mu\text{m}$ amorphous silicate band dominates the spectrum. Thus, we have not included this material in our study.

5.1. The $23\text{--}24\mu\text{m}$ dust band

In crystalline olivine, although the absorption peaks are mostly contributed by Si–O–Si stretching and O–Si–O bending vibrations up to around $20\mu\text{m}$, translational motions of metal cations within the oxygen cage and complex translations involving metal and Si atoms lead to complex bands beyond $21.28\mu\text{m}$ (more details in e.g., Servoin & Piriou 1973; Dorschner & Henning 1986; Hofmeister 1997; Henning et al. 2005). Iron plays an important role in the wavelength region between 23 and $24\mu\text{m}$ (e.g., Jäger et al. 1998; Koike et al. 2003; Tamanai & Mutschke 2010). As the amount of iron increases in olivine, this $23\text{--}24\mu\text{m}$ band undergoes a redshift up to the iron content of 40%. However, the intensity of this peak weakens beyond this point. When the iron content exceeds 60%, this peak is no longer visible (Koike et al. 2003). For instance, Tamanai & Mutschke (2010) showed that forsterite has a peak at $23.27\mu\text{m}$ whereas this peak is located at $23.91\mu\text{m}$ for 20% iron content of olivine based on Aerosol

spectra. Thus, the position of this peak gives us a clue to the presence of iron in olivine dust grains.

We pay attention to the peak around $23\text{--}24\mu\text{m}$ of the MIRI spectrum. By fitting a 1D Gaussian curve, the peak position is located at $23.44\mu\text{m}$. Likewise, we also derive the peak from the Spitzer data which is found to be $23.47\pm 0.01\mu\text{m}$. The fitted $23\text{--}24\mu\text{m}$ band and the peak positions of the full spectral resolution MIRI spectrum and rebinned MIRI spectrum ($R=500$) are shown in Fig. 5. The rebinned spectrum is the one used for dust fitting. These results correspond to a 10% iron content olivine, which has its peak situated at $23.46\mu\text{m}$ (Tamanai & Mutschke 2010). We note that the error on the measured wavelength does not include systematic errors resulting from slightly different choices of the underlying continuum.

5.2. Dust fitting with Fe-rich silicate dust

In addition to Model GRF, we also fitted the MIRI spectrum with Fe-rich silicate species, including fayalite, amorphous MgFeSiO_4 , and amorphous $\text{MgFeSi}_3\text{O}_6$, and we refer to this as Model Mg+Fe. The model agrees well with the MIRI spectrum, and the mean residual is 1.1%, as shown in Fig. 6. Within this model, enstatite and fayalite are found to be less than 1% in mass fraction, and we exclude those dust species from the figure. The model fit retrieves large Fe-rich amorphous silicate grains, while pure Mg amorphous silicates are more favored for small grains.

Large amorphous silicates have broad and weak band resonances and weak flux contributions compared to small amorphous and crystalline silicates, but the mass fraction is proportional to the grain size retrieved. Thus, small flux contributions from the large grains can result in large mass contributions. However, we did not find a satisfactory fit to the MIRI spectrum using only Fe-rich silicates, i.e. excluding pure Mg silicates. These results demonstrate that pure Mg silicates are required to fit the spectrum and dominate the PDS 70 disk, while the amount of Fe-rich silicate is still ambiguous.

6. Dust fitting for Spitzer data

We also fitted the Spitzer spectrum with GRF opacities in two ways: 1) the same wavelength range with the MIRI spectrum (Model Spitzer), 2) the full wavelength range of Spitzer spectrum (Model Spitzer(full)). The results of Model Spitzer and Model Spitzer(full) are shown in the right panel of Fig. 4 and Fig. A.3, respectively. Because the Spitzer covers a broader wavelength range than MIRI, we allow the DuCK to constrain temperature gradient across the disk surface rather than assuming a single temperature in Model Spitzer(full). The temperatures are shown in Fig. 3.

The inner rim temperatures derived from both Spitzer spectrum fittings are significantly higher than that obtained from the MIRI spectrum, reaching the upper limit, 1500 K, of our temperature priors in DuCK. We did not raise the upper limit because silicate dust sublimates above $\sim 1500\text{ K}$ (Duschl et al. 1996; Kama et al. 2009). We note that the precise inner rim temperature does not affect the analysis of dust mineralogy in the disk surface. The higher inner rim temperature derived from the Spitzer spectrum compared to the MIRI spectrum can be attributed to the differences in their flux at short wavelengths. The Spitzer spectrum has a higher flux around $5\mu\text{m}$, which is more sensitive to the hotter inner regions of the disk. In contrast to the inner rim, the disk surface temperature derived from the Spitzer spectrum is cooler than the MIRI spectrum because of the lower

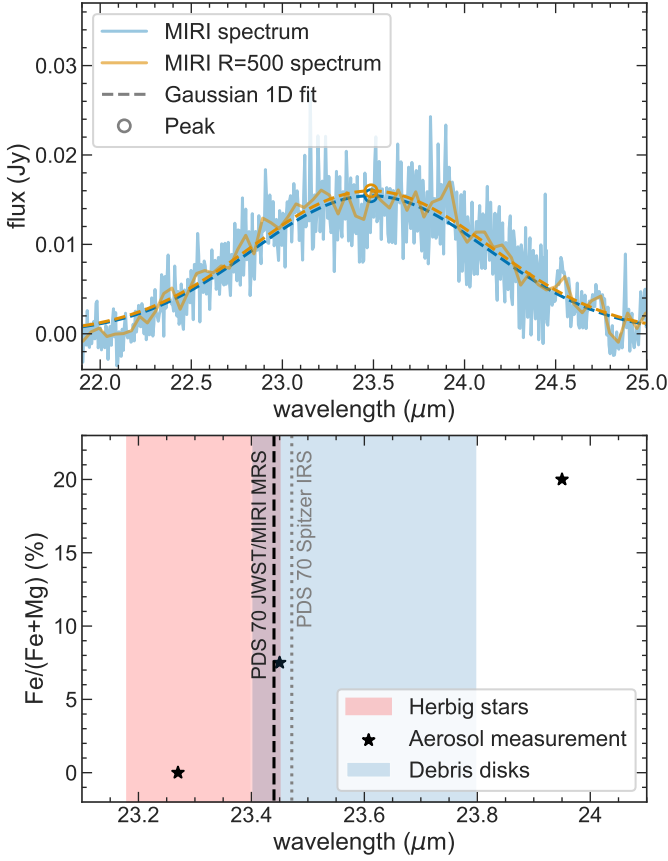


Fig. 5: Measurement of the 23-24 μm band peak. The MIRI spectrum was fitted with a 1D gaussian curve (blue dashed line) and found the peak at 23.4 μm (blue circle) in the upper panel. MIRI spectrum with R=500 is also plotted and fitted with the 1D gaussian curve (yellow solid and dashed lines), and the gaussian curve also peaks at 23.4 μm (yellow circle). Lower panel shows the locations of the peaks for the MIRI and Spitzer spectra together with Aerosol measurements. Regions where the peaks locate for Herbig Ae/Be stars and debris disks are shaded in red and blue, respectively.

flux around the 10 μm silicate band, where warm dust dominates, and the increased flux at longer wavelength, where colder dust contributes.

Both models indicate that amorphous silicates (Mg_2SiO_4 and MgSiO_3) with sizes ranging from 0.1 to 1 μm make up 85 % of the total mass fraction in the disk surface. Crystalline silicates still do not show evidence of enstatite, but forsterite is clearly detected. Model Spitzer identifies only 1 and 2 μm forsterite grains with a mass fraction of ~ 10 % while Model Spitzer(full) finds 0.1, 1, 2, and 5 μm forsterite grains. Because of the large 5 μm sized grains, Model Spitzer(full) has a higher mass fraction of forsterite at ~ 15 % in total. The values are summarized in Table A.1.

Both MIRI and Spitzer spectra show a dominance of amorphous silicates (Mg_2SiO_4 and MgSiO_3), contributing ~ 80 % of the total mass fraction with a preference for SiO_3 stoichiometry. However, the model describing MIRI spectrum shows larger grain sizes, typically a few microns, compared to the model for Spitzer spectrum, which is dominated by 0.1 μm grains. In addition, the crystallinity derived from the MIRI spectrum

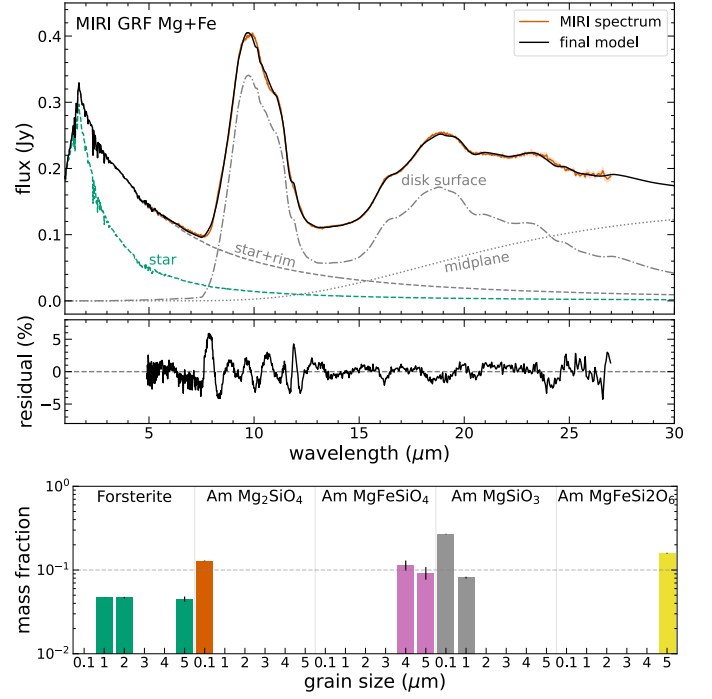


Fig. 6: Fitting with additional Fe-rich dust GRF opacities from Model GRF. Overall fitting result is as good as Model GRF, especially beyond 14 μm . Mass fractions are only shown for dust species detected greater than 1 %.

ranges around 10-20 %, depending on given largest grains, while Spitzer spectrum shows around 10-15 % crystallinity.

We also measured the mass of 0.1 μm amorphous MgSiO_3 in the disk surface with

$$M_{\text{dust}} = \frac{F(\nu)d^2}{B(\nu, T)\kappa(\nu)}, \quad (3)$$

where $F(\nu)$ is the flux from the amorphous MgSiO_3 in the disk surface, d is the distance to PDS 70, $\kappa(\nu)$ is the opacity of 0.1 μm amorphous MgSiO_3 , $B(\nu, T)$ is the Planck function at frequency ν , and the single disk surface temperature T . We find $4.5 \times 10^{-7} M_{\oplus}$, which is 32.8 % of total dust mass in the inner disk surface, as the result of Model GRF, so the total dust mass in the inner disk surface is $1.37 \times 10^{-6} M_{\oplus}$. In Spitzer spectrum, amorphous MgSiO_3 is $4.8 \times 10^{-7} M_{\oplus}$, which is 37.6 % of the total dust mass in the disk surface, so the total dust mass is $1.27 \times 10^{-6} M_{\oplus}$. The dust mass in the inner disk surface is similar between MIRI and Spitzer spectra. We note that only a small fraction of the total dust mass is in the disk surface, and Benisty et al. (2021) infer the total dust mass within 18 au as 0.08 – 0.36 M_{\oplus} .

7. Discussion

Our fitting results agree on the dominance of small amorphous silicates and the lack of enstatite, and we found around or less than 10 % iron content in crystalline silicates. Moreover, the variability of PDS 70 between JWST/MIRI MRS and Spitzer IRS can be seen in Fig. 1 and is also reported in Perotti et al. (2023). In this section, we discuss iron content in crystalline silicates in Sect. 7.1, the absence of enstatite in Sect. 7.2, the variability between MIRI and Spitzer data in Sect. 7.3, and the origins of small silicate dust in Sect. 7.4.

7.1. Iron content in crystalline silicates

We find that crystalline silicates in the PDS 70 disk contain up to $\sim 10\%$ of iron based on the peak position of the $23\text{--}24\text{ }\mu\text{m}$ band. We note that in our theoretical grain shape models (e.g., GRF), the peak position shifts toward longer wavelengths with increasing grain size, as shown in Fig. C.1. That would imply that the Aerosol-derived iron content - based on $\sim 1\text{ }\mu\text{m}$ sized grains - is in fact an upper limit. However, Aerosol experiments using samples of larger forsterite grains (Tamanai & Mutschke 2010) do not show a shift of the $23\text{ }\mu\text{m}$ band to longer wavelengths, i.e. different from the GRF grain model results. Taken together, we conclude that the iron content in the crystalline olivine is likely around or less than 10% . We note that we do not consider scattering opacities, which become important for optically thick dust clouds and large grains (a few microns). However, our analysis shows the dust observed in PDS 70 is dominated by optically thin, relatively small grains ($\sim 1\text{ }\mu\text{m}$), so we only consider absorption coefficients in this study.

It is interesting to compare the iron content in olivines in the PDS 70 disk to that found in gas-rich protoplanetary disks and debris disks. Juhász et al. (2010) and Olofsson et al. (2010) found that Spitzer IRS spectra of Herbig Ae/Be and T-Tauri stars can be well fitted using forsterite, with only a handful of disks requiring iron-containing olivines. Limits on the iron content of less than 2% in olivine were found in the outer disks of the Herbig Ae/Be stars and T-Tauri stars, using Herschel detection of the $69\text{ }\mu\text{m}$ band (Sturm et al. 2013). In warm debris disks like HD69830 and HD113766A, the presence of 20% iron-containing olivine has been reported in Tamanai & Mutschke (2010); Olofsson et al. (2012). In contrast, de Vries et al. (2012) constrained the iron content in olivine in the cold debris disk of β Pic to be 1% . These observations suggest that cold outer-disk olivines in gas-rich disks and debris disks are very iron-poor, while warm inner-disk olivines in gas-rich disks are generally very iron-poor but may contain some iron in warm debris disks, reaching the values up to 20% . Our limits on the iron content in olivines in the PDS 70 disk are consistent with those typical for the inner regions of gas-rich disks.

7.2. Lack of enstatite

Remarkably, we find no evidence for warm inner disk enstatite, but enstatite has been detected in many other inner disks. Bouwman et al. (2008) investigated crystalline silicates in seven T-Tauri disks observed by Spitzer IRS and found that the inner warm dust at $\sim 1\text{ au}$ is more enstatite-rich, while the cold outer disk (around $5\text{--}15\text{ au}$) is more rich in forsterite. Juhász et al. (2010) found that mid-infrared spectra of Herbig Ae/Be stars observed by Spitzer tend to show a higher abundance of enstatite than forsterite when analysing the shorter wavelength regions ($7\text{--}17\text{ }\mu\text{m}$), representing the inner disk, while it is vice versa in the longer wavelength region ($17\text{--}35\text{ }\mu\text{m}$), representing the outer disk (Jang et al. 2024). Olofsson et al. (2010) analyzed the dust composition of 58 T-Tauri disks observed with Spitzer IRS and found a similar fractions of forsterite and enstatite in the inner disk and a higher fraction of forsterite in the outer disk. Thus, in the inner gas-rich disks, enstatite is relatively abundant compared to the outer disk.

Interestingly, Harker et al. (2023) show that typical mass ratios of enstatite to forsterite in solar system comets observed by Spitzer are similar or greater than 1, but with large variations between individual comets. This could indicate that, in the comet forming region of the proto-solar nebula, significant reservoirs

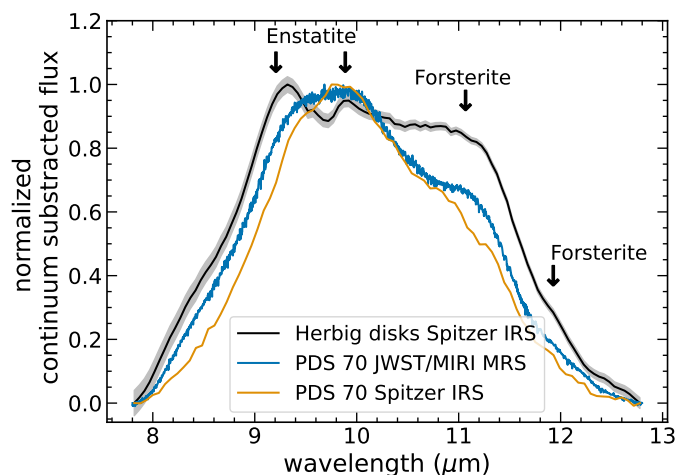


Fig. 7: The $10\text{ }\mu\text{m}$ silicate band of the MIRI (blue) and Spitzer (orange) spectra of PDS 70 compared to 9 Herbig Ae/Be stars, observed by Spitzer IRS (gray). The arrows at $9.2\text{ }\mu\text{m}$ and $9.8\text{ }\mu\text{m}$ indicate the enstatite bands, while the arrows at $11\text{ }\mu\text{m}$ and $11.9\text{ }\mu\text{m}$ indicate the forsterite bands based on GRF opacities.

of both forsterite and enstatite were present. The building blocks of comets consist of small micron-sized grains, and the temperatures of comets are too low for parent-body processing. The Stardust mission that returned samples from the comet Wild 2 contained both forsterite and enstatite (Brownlee 2014). All taken together, these findings show that small enstatite grains can be present in the icy regions of protoplanetary disks.

However, in most of our retrievals of MIRI and Spitzer spectra of PDS 70, enstatite is not detected except for Model Aerosol. Model Aerosol has limitations in grain sizes and is not well fitted with the spectrum. The high abundance of inner-disk enstatite found in previous studies of other disks was based on fitting of the short wavelength $5\text{--}17\text{ }\mu\text{m}$ Spitzer IRS spectra. This range contains both the strong $9.3\text{ }\mu\text{m}$ enstatite band, as well as weaker bands near $14\text{--}15\text{ }\mu\text{m}$. These latter bands would be sensitive to the detection of enstatite in the spectrum. This can affect the outcome of our analysis. Thus, we also attempted to fit the MIRI spectrum from $5\text{ }\mu\text{m}$ to $13\text{ }\mu\text{m}$, where a strong enstatite band appears at $9.3\text{ }\mu\text{m}$ regardless of the $14\text{ }\mu\text{m}$ bands. We find that enstatite remains undetected. In addition, we compared the $10\text{ }\mu\text{m}$ silicate band in the MIRI and Spitzer spectra with the Spitzer IRS observations of 9 Herbig disks in Juhász et al. (2010). A linear continuum from $7.8\text{ }\mu\text{m}$ to $12.8\text{ }\mu\text{m}$ was subtracted from the $10\text{ }\mu\text{m}$ silicate band, which were then normalized to obtain the shapes, as shown in Fig. 7. The black solid line represents the median of the 9 Herbig disks, with the shaded area indicating the standard deviation. Herbig disks are known to be enstatite-rich based on the prominent enstatite band at $9.3\text{ }\mu\text{m}$ (Juhász et al. 2010). In Fig. 7, both MIRI and Spitzer spectra do not show the enstatite band as in the Herbig disks. Thus, we conclude that micron-sized dust grains in the inner PDS 70 disk are depleted in enstatite.

7.3. Variability of the inner disk dust

Gaidos et al. (2024) show that the PDS 70 disk flux varies from $\sim 200\text{ mJy}$ to $\sim 1\text{ mJy}$ at 3.4 and $4.6\text{ }\mu\text{m}$ using NEOWISE photometry over ~ 12 years, indicating that the innermost hottest dust can either appear or disappear entirely. Moreover, their

photosphere-subtracted best-fit model suggest around 50 % of the disk contribution around $5 \mu\text{m}$, in agreement with Perotti et al. (2023). In both MIRI and Spitzer spectra, our fit shows the disk contribution to be ~ 60 % of the flux, suggesting that we may be detecting PDS 70 during a phase where the inner disk contribution is transitioning between complete appearance and disappearance. The factor of 100 flux variation in this strong near-infrared variability is most easily explained by variations of the amount of optically thin hot dust in the innermost disk.

As the bulk of hot dust appears and disappears, it provides a variable innermost disk opacity. This can affect the temperature of dust at larger distances and may provide a natural explanation of the temperature differences between the MIRI and Spitzer spectra. We can derive a rough distance of this warm dust using the following expression:

$$\frac{T_{\text{dust}}}{T_{\text{star}}} = \left(\frac{r}{R_{\text{star}}} \right)^{-0.5} \quad (4)$$

and using the stellar temperature and the disk surface temperature derived above. This gives a distance of about 0.47 au. The Spitzer spectrum shows larger infrared excess around $5 \mu\text{m}$ compared to the MIRI spectrum, which could indicate a more obscured innermost disk. Thus, the implication is that the temperature variations are probably not due to a difference in radial distance from the star, but are the result of varying irradiation of a stationary optically thin dust cloud. Due to this dust cloud in the innermost disk, radiation from the star is blocked, so the dust at larger radial distances can be cooler; the fitting results show that the disk surface temperature in the Spitzer spectrum is lower than in the MIRI spectrum in Fig. 3.

The range of midplane temperatures in both MIRI and Spitzer spectra are similar (third panel of Fig. 3). The midplane temperature in Model Spitzer falls within the temperature range of Model GRF, and Model Mg+Fe is very similar to Model Spitzer at ~ 140 K. Thus, the variability at wavelengths beyond $15 \mu\text{m}$, where the optically thick midplane component in the model starts to contribute to the spectrum, is not due to a temperature difference, and does not follow the same trend as found for the optically thin dust component. One approach to increase the flux at longer wavelengths is to increase the amount of cold emitting dust.

Despite the differences in temperatures and flux levels, the optically thin dust mass does not vary between MIRI and Spitzer spectra. In Model Spitzer, we found smaller dust grains compared to the MIRI spectra, and these smaller grains increase the dust surface area while maintaining the same dust mass. Dust evolution over the observation time from Spitzer to MIRI (~ 15 years) could possibly explain the variability, as the grain growth timescale is 1.8 years at 1 au ($\tau_{\text{grow}} = 1/\epsilon\Omega_K$ Birnstiel et al. 2016, where ϵ is the dust-to-gas ratio of 0.1 in the inner disk Portilla-Revelo et al. 2023). Thus, the PDS 70 disk at the time of the Spitzer observation possibly had more cold and small dust, compared to the epoch of the MIRI observations.

7.4. Origin of the inner disk small grains

The PDS 70 disk likely represents the later stages of protoplanetary disk evolution, when accreting planets are formed. As the disk evolves, dust grains grow into larger bodies, such as pebbles or planetesimals, and dust gets depleted in the inner disk due to accretion onto the star. Due to the large gap in the PDS 70 disk and the resulting pressure bump in the outer disk (~ 77 au; Pinilla et al. 2024), a continuous supply of dust from

the outer disk is limited. Thus, the inner disk is expected to be dust-depleted, and the ALMA observation as well as detailed radiative transfer models indeed show a highly dust-depleted inner disk (Benisty et al. 2021; Portilla-Revelo et al. 2023). However, mid-infrared observations of the PDS 70 disk show that the inner disk emission is strongly dominated by sub-micron-sized grains, more than most other disks observed so far. It is, therefore, interesting to discuss the possible origins of this abundant small grain component. We consider two scenarios to understand the origin of the small grains: 1) locally produced grains, either resulting from annealing or gas phase condensation or collisions among planetesimals, in the dynamical inner disk and 2) dust drifting inward from the outer disk. We discuss these two possibilities in the context of the dust composition derived in this study.

7.4.1. Local production

Small crystalline silicate grains can be locally produced in the inner disk as a result of the fragmentation of parent bodies or by gas phase condensation. In the case of gas phase condensation, the formation of both forsterite and enstatite can be expected if conditions for chemical equilibrium apply for a solar composition gas (Woitke et al. 2018). This is not what we observe. There are several possibilities to suppress the formation of enstatite. Deviations from chemical equilibrium may result in the freeze-out of the reaction to form enstatite. Such an effect can, for instance, explain the formation of forsterite rather than enstatite during the flaring event in EX Lupi (Ábrahám et al. 2019). A second way to avoid the formation of enstatite is by lowering the gas phase abundance of silicon (Jorge et al. 2021).

The small crystalline silicate grains can also be the result of parent-body processing and their release from these parent bodies through collisions. The presence of two gas giant planets in the outer gap and the highly variable inner-disk dust reservoir suggest that the PDS 70 disk is in an advanced stage of planet formation and inner-disk clearing. If the observed crystalline silicate grains in the inner disk are due to parent-body collisions, these parent bodies must be rich in forsterite. In addition, their low iron abundance suggests these parent bodies did not experience a high level of oxidation. Remarkably, Olofsson et al. (2012) found a lack of enstatite from an analysis of small warm dust grains in debris disks. However, these grains contained significant amounts of iron. The grains we detect in the PDS70 disk, from a point of view of their iron content, are more in line with the iron-poor grains usually found in gas-rich protoplanetary disks. In the next subsection, we discuss another possibility for the origin of the crystalline silicates in the context of the pressure bump in the outer disk.

7.4.2. Filtration

The PDS 70 disk has a 54-au gap with two giant exoplanets, which produce a pressure bump at the outer edge of the gap. This pressure bump traps the drifting dust that is decoupled from the gas. However, small grains, which are more coupled to the gas, can penetrate the pressure bump and drift toward the inner disk. This is called filtration.

Filtration at the outer edge of the gap may explain the presence of only forsterite for crystalline silicates in the disk. Pinilla et al. (2024) model the dust evolution in the PDS 70 disk, using radiative transfer simulations to investigate the existence of an inner disk with the two giant planets in the gap. They suggest that small dust ($< 0.1 \mu\text{m}$) is supplied by continuous fragmen-

tation of trapped dust in the pressure bump. These small dust grains penetrate the pressure bump and supply dust to the inner disk. Although the inner disk of PDS 70 may have been initially enstatite-rich like other observed T Tauri disks in Bouwman et al. (2008); Olofsson et al. (2010), the enstatite could have been accreted into the central star due to a short accretion timescale. During this depletion of enstatite, small forsterite grains penetrate the pressure bump from the outer disk, which is forsterite-rich (Bouwman et al. 2008; Juhász et al. 2010; Olofsson et al. 2010), travel to the inner disk, and replenish the inner disk. Eventually, crystalline silicates in the inner disk could become dominated by forsterite. This process is schematically shown in Fig. 8.

Observations indicate that outer disks are more forsterite-rich, but the origin of this mineralogical gradient is not well understood. Gail (2004) in fact predicts an opposite trend, with an enstatite-rich outer disk resulting from the conversion of innermost forsterite to enstatite as small grains in the midplane are mixed outward. The freeze-out of the reaction that converts forsterite to enstatite may prevent this process. Interestingly, the EX Lupi outburst reported by Ábrahám et al. (2019) shows the production of only forsterite in the heated upper disk layers. These observations also indicate that the freshly formed forsterite was transported outward. If young stars experience frequent outbursts, this might provide a mechanism to enrich the outer disk with forsterite.

While the penetrating small grains travel toward the inner disk, they grow to millimeter or centimeter-sized dust grains over 1 Myr (Pinilla et al. 2024). The dust evolution models result in a power-law index of the grain size distribution as ~ 3 , indicating fewer small grains ($0.1 \mu\text{m}$) and more large grains ($\sim 10\text{--}100 \mu\text{m}$) at 5, 10, 15 au, compared to the observed size distribution of interstellar grains (MRN distribution; Mathis et al. 1977) at 10 au. These models suggest larger grain sizes than our best fit to MIRI spectrum. Theoretical simulations of grain growth through collisions (Dominik & Dullemond 2024) during its inward drifting (Pinilla et al. 2016, 2024) suggest that grain sizes could grow to tens of microns or even centimeters.

Dominik & Dullemond (2024) show that the size distribution of dust grains becomes close to monodisperse around a few centimeters. On the other hand, Gaidos et al. (2024) suggest a power-law index to be 3.5–4 based on 0.4m-LCOGT observations of the PDS 70 disk, which aligns with our finding of a few microns as the maximum grain size. The size distribution is smaller than what simulations predict, which only include collisional sticking, bouncing, and fragmentation. One possible explanation is fragmentation of icy grains after crossing the ice line. Pinilla et al. (2024) do not consider the fragmentation of the grains into smaller sizes, leading to an overestimation of the grain size in the inner disk.

Throughout the dust growth process, grains may accumulate ices beyond their ice lines. When centimeter-sized icy pebbles cross the ice line, the ice sublimates, causing the dust aggregates to break apart into smaller dust grains. This process is described in the many-seeds scenario by Schoonenberg & Ormel (2017), and also suggested as a possibility for the PDS 70 disk in Perotti et al. (2023). Houge et al. (2024) simulate grain growth in the many-seeds scenario and compare their results with ALMA observations of the V883 Ori disk. In their simulation, the ice line moves outward from 3 au to 80 au due to outburst events rather than dust drifting inward and passing the ice line. However, we can still discuss how icy dust responds when it crosses the ice line. In the many-seeds scenario, water ice trapped in dust sublimates, so the dust breaks apart into micron-sized grains. This change in grain size reduces the fragmentation barrier (Birnstiel

et al. 2011), which suppresses re-coagulation. Thus, the many-seed scenario may explain why the inner disk of the PDS 70 is dominated by sub-micron to micron-sized dust.

Warm H_2O has been detected in the MIRI spectrum and is well fitted by a slab model at 600 K within 0.05 au (Perotti et al. 2023). Pinilla et al. (2024) suggest that small grains can shield UV radiation, which prevents H_2O photodissociation (Heays et al. 2017), and enriches the inner disk through the filtration mechanism. We note that Pinilla et al. (2024) do not include UV photochemistry in their model. The water supply in the inner disk can be explained by the sublimation of ices in pebbles that have grown after penetrating the pressure bump and break apart at the ice line. A second possibility is the drift of oxygen gas through the gap, followed by efficient water formation in the warm and dense inner disk (Perotti et al. 2023; Portilla-Revelo et al. 2023). Pinilla et al. (2024) discuss that the initial inner disk is accreted within the first million years of the dust evolution, and the dust from the outer disk starts to replenish the inner disk in the 1–3.5 Myr range. Because the age of PDS 70 is estimated to be $\sim 5.4 \pm 1$ Myr (Keppler et al. 2018), filtration and fragmentation may still be ongoing. This implies that the observed dust in the PDS 70 disk is more likely to be primitive rather than the result of parent-body processing.

Finally, we note that both the filtration mechanism as well as collisions between parent bodies can contribute to the inner disk small grain population. Local production of crystalline silicates via flash heating or shock heating could enhance the crystallinity of small dust in the inner disk while depleting enstatite. While forsterite grains form locally in the inner disk, small forsterite grains from the outer disk penetrate the pressure bump and re-supply the inner disk. These forsterite grains may fragment upon crossing the ice line and become sub-micron sized as we discussed above.

8. Conclusion

We have analysed the PDS 70 spectrum recently obtained by JWST/MIRI MRS, and archival Spitzer IRS spectrum, using the dust fitting model DuCK (Kaeufer et al. 2024). DuCK employs a two-layer disk model described in Juhász et al. (2009, 2010) and uses the MultiNest algorithm to identify the best model through retrieval with the dust mass fractions determined by the non-negative least squares fitting. We find that the MIRI spectrum can be fitted with a single temperature for the optically thin disk surface. We use three different types of absorption efficiencies: GRF, DHS, and Aerosol. The outcome of the fitting procedure is dependent on the choice of opacities, with GRF providing the best fitting model to the spectrum. Thus, this dependency should be kept in mind for future dust retrievals. We summarize our conclusions as follows:

- Small amorphous silicates are the major dust species in the PDS 70 inner disk and dominate the spectra. The strength of the optically thin $10 \mu\text{m}$ silicate band is exceptionally strong, and any contribution of optically thick dust is minor at those wavelengths. This is different from most other observed disks.
- The model with GRF dust opacities provides the best fit to the observations.
- The silicate dust in the PDS 70 disk is dominated by Mg-rich silicates. The analysis of the 23–24 μm band suggests around or less than $\sim 10\%$ iron content in crystalline silicates, and dust fitting with both pure Mg silicates and Fe-rich silicates results in no detection of Fe-rich silicates or only in the large

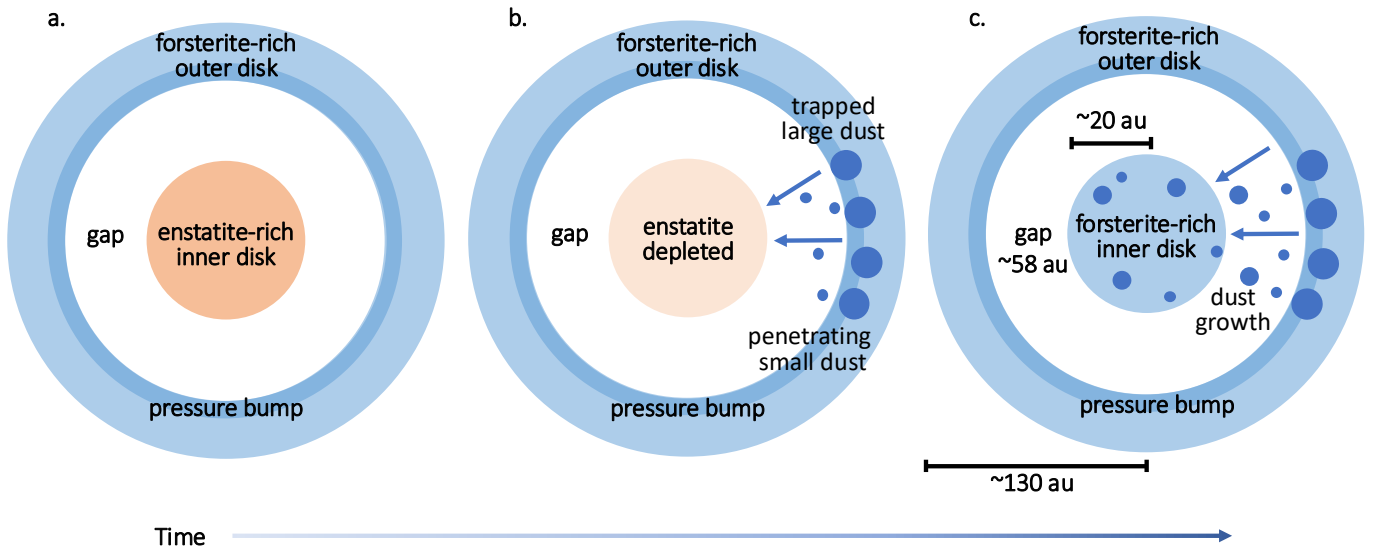


Fig. 8: Sketch of the filtration mechanism in the PDS 70 disk. (a) The disk has a gap between the inner and outer disks. The inner disk is initially enstatite-rich, and the outer disk forsterite-rich. (b) While enstatite is depleted in the inner disk due to accretion onto the central star, small dust that penetrates the pressure bump travels through the gap to the inner disk. (c) The small dust supply the inner disk, and the inner disk eventually becomes forsterite-rich.

dust grains of Fe-rich silicate. The iron may be in metallic form, which our analysis is not sensitive to.

- In Model GRF and DHS, we find no evidence for enstatite, and Model Aerosol shows enstatite at 2 %. Forsterite is detected in range of 4–20 %.
- The Spitzer spectrum, taken 15 years earlier, shows dust mineralogy similar to the MIRI spectrum, but the grain sizes are smaller and colder at roughly the same optically thin dust mass. This could indicate grain growth over the ~ 15 years time span between the Spitzer and MIRI observations.
- The temperature difference of the optically thin silicate dust between MIRI and Spitzer spectra may be due to a change in the innermost disk opacity, resulting in variations of the flux received by the star at the same physical distance. This is likely due to a dynamic innermost disk, as also evidenced by the strong near-IR variability (Gaidos et al. 2024).
- Although the variability beyond $15 \mu\text{m}$ is not well understood and requires radiative transfer modeling, it could be due to higher abundances of small dust grains at large distances in Spitzer spectrum, which increases the emitting surface of cold dust.
- The low abundance of enstatite and the iron-poor nature of crystalline silicates suggest that the small grains in the inner disk are more likely the result of the filtration and inward drift of small grains from the outer disk. Such grains may also transport water to the inner disk and fragment at the snow line. However, collisions of enstatite-depleted parent bodies and local heating processes can still produce the inner disk dust grains.

Iron can exist in featureless dust species such as metallic iron or FeS, despite the iron-poor silicate dust species. Besides iron, other featureless dust species like amorphous carbon were also not accounted for this study. Investigating these species in the disk is a topic for future study, helping us to understand the iron and carbon content in planets. Moreover, the dust opacities depend on the provided optical constants. Expanding our study by including different sets of optical constants for GRF particle

shapes could provide a better fit, especially near $8 \mu\text{m}$. Because dust fitting results depend on the shape of opacities, different sets of optical constants should also be investigated.

Acknowledgements. This work is based on observations made with the NASA/ESA/CSA James Webb Space Telescope. The data were obtained from the Mikulski Archive for Space Telescopes at the Space Telescope Science Institute, which is operated by the Association of Universities for Research in Astronomy, Inc., under NASA contract NAS 5-03127 for JWST. These observations are associated with program #1282. The following National and International Funding Agencies funded and supported the MIRI development: NASA; ESA; Belgian Science Policy Office (BELSPO); Centre Nationale d’Etudes Spatiales (CNES); Danish National Space Centre; Deutsches Zentrum für Luft- und Raumfahrt (DLR); Enterprise Ireland; Ministerio De Economía y Competividad; Netherlands Research School for Astronomy (NOVA); Netherlands Organisation for Scientific Research (NWO); Science and Technology Facilities Council; Swiss Space Office; Swedish National Space Agency; and UK Space Agency. We acknowledge to Combined Atlas of Sources with Spitzer IRS Spectra (CASSIS) database for the use of low-resolution spectra. V. C. thanks the Belgian F.R.S.-FNRS, and the Belgian Federal Science Policy Office (BELSPO) for the provision of financial support in the framework of the PRODEX Programme of the European Space Agency (ESA) under contract number 4000142531. G.P. gratefully acknowledges support from the Max Planck Society. E.v.D. acknowledges support from the ERC grant 101019751 MOLDISK and the Danish National Research Foundation through the Center of Excellence “InterCat” (DNRF150). T.H. and K.S. acknowledge support from the European Research Council under the Horizon 2020 Framework Program via the ERC Advanced Grant Origins 83 24 28. I.K., A.M.A., and E.v.D. acknowledge support from grant TOP-1 614.001.751 from the Dutch Research Council (NWO). B.T. is a Laureate of the Paris Region fellowship program, which is supported by the Ile-de-France Region and has received funding under the Horizon 2020 innovation framework program and Marie Skłodowska-Curie grant agreement No. 945298. D.G. thanks the Belgian Federal Science Policy Office (BELSPO) for the provision of financial support in the framework of the PRODEX Programme of the European Space Agency (ESA). M.T. acknowledges support from the ERC grant 101019751 MOLDISK. D.B. has been funded by Spanish MCIN/AEI/10.13039/501100011033 grants PID2019-107061GB-C61 and No. MDM-2017-0737.

References

- Ábrahám, P., Chen, L., Kóspál, Á., et al. 2019, *ApJ*, 887, 156
Aoyama, Y. & Ikoma, M. 2019, *ApJ*, 885, L29
Apai, D., Pascucci, I., Bouwman, J., et al. 2005, *Science*, 310, 834

- Argyriou, I., Glasse, A., Law, D. R., et al. 2023, *A&A*, 675, A111
- Baron, E., Chen, B., & Hauschildt, P. H. 2010, PHOENIX: A General-purpose State-of-the-art Stellar and Planetary Atmosphere Code, Astrophysics Source Code Library, record ascl:1010.056
- Benisty, M., Bae, J., Facchini, S., et al. 2021, *ApJ*, 916, L2
- Birnstiel, T., Fang, M., & Johansen, A. 2016, *Space Sci. Rev.*, 205, 41
- Birnstiel, T., Ormel, C. W., & Dullemond, C. P. 2011, *A&A*, 525, A11
- Blakely, D., Johnstone, D., Cugno, G., et al. 2024, *arXiv e-prints*, arXiv:2404.13032
- Bouwman, J., Henning, T., Hillenbrand, L. A., et al. 2008, *ApJ*, 683, 479
- Bouwman, J., Meeus, G., de Koter, A., et al. 2001, *A&A*, 375, 950
- Bradley, J. P., Brownlee, D. E., & Veblen, D. R. 1983, *Nature*, 301, 473
- Brownlee, D. 2014, *Annual Review of Earth and Planetary Sciences*, 42, 179
- Bushouse, H., Eisenhamer, J., Dencheva, N., et al. 2023, JWST Calibration Pipeline
- Campbell-White, J., Manara, C. F., Benisty, M., et al. 2023, *ApJ*, 956, 25
- Chiar, J. E. & Tielens, A. G. G. M. 2006, *ApJ*, 637, 774
- Christiaens, V., Gonzalez, C., Farkas, R., et al. 2023, *The Journal of Open Source Software*, 8, 4774
- Christiaens, V., Samland, M., Gasman, D., Temmink, M., & Perotti, G. 2024a, MINDS: Hybrid pipeline for the reduction of JWST/MIRI-MRS data, Astrophysics Source Code Library, record ascl:2403.007
- Christiaens, V., Samland, M., Henning, T., et al. 2024b, *A&A*, 685, L1
- Colangeli, L., Henning, T., Brucato, J. R., et al. 2003, *A&A Rev.*, 11, 97
- de Vries, B. L., Acke, B., Blommaert, J. A. D. L., et al. 2012, *Nature*, 490, 74
- Dominik, C. & Dullemond, C. P. 2024, *A&A*, 682, A144
- Dorschner, J., Begemann, B., Henning, T., Jäger, C., & Mutschke, H. 1995, *A&A*, 300, 503
- Dorschner, J. & Henning, T. 1986, *Ap&SS*, 128, 47
- Duschl, W. J., Gail, H. P., & Tscharnuter, W. M. 1996, *A&A*, 312, 624
- Espaillet, C., Furlan, E., D'Alessio, P., et al. 2011, *ApJ*, 728, 49
- Fabian, D., Henning, T., Jäger, C., et al. 2001, *A&A*, 378, 228
- Feroz, F. & Hobson, M. P. 2008, *MNRAS*, 384, 449
- Feroz, F., Hobson, M. P., Cameron, E., & Pettitt, A. N. 2019, *The Open Journal of Astrophysics*, 2, 10
- Feroz, F., Hobson, M. P., Zwart, J. T. L., Saunders, R. D. E., & Grainge, K. J. B. 2009, *MNRAS*, 398, 2049
- Forrest, W. J., Sargent, B., Furlan, E., et al. 2004, *ApJS*, 154, 443
- Furlan, E., Hartmann, L., Calvet, N., et al. 2006, *ApJS*, 165, 568
- Gaidos, E., Thanathibodee, T., Hoffman, A., et al. 2024, *arXiv e-prints*, arXiv:2403.09970
- Gail, H. P. 2004, *A&A*, 413, 571
- Gomez Gonzalez, C. A., Wertz, O., Absil, O., et al. 2017, *AJ*, 154, 7
- Haffert, S. Y., Bohn, A. J., de Boer, J., et al. 2019, *Nature Astronomy*, 3, 749
- Harker, D. E., Wooden, D. H., Kelley, M. S. P., & Woodward, C. E. 2023, *PSJ*, 4, 242
- Hashimoto, J., Aoyama, Y., Konishi, M., et al. 2020, *AJ*, 159, 222
- Hashimoto, J., Dong, R., Kudo, T., et al. 2012, *ApJ*, 758, L19
- Hashimoto, J., Tsukagoshi, T., Brown, J. M., et al. 2015, *ApJ*, 799, 43
- Heays, A. N., Bosman, A. D., & van Dishoeck, E. F. 2017, *A&A*, 602, A105
- Henning, T. 2010, *ARA&A*, 48, 21
- Henning, T., Kamp, I., Samland, M., et al. 2024, *PASP*, 136, 054302
- Henning, T. & Mutschke, H. 1997, *A&A*, 327, 743
- Henning, T., Mutschke, H., & Jäger, C. 2005, in *Astrochemistry: Recent Successes and Current Challenges*, ed. D. C. Lis, G. A. Blake, & E. Herbst, Vol. 231, 457–468
- Henning, T. & Stognienko, R. 1996, *A&A*, 311, 291
- Hofmeister, A. M. 1997, *Physics and Chemistry of Minerals*, 24, 535
- Houge, A., Macías, E., & Krijt, S. 2024, *MNRAS*, 527, 9668
- Isella, A., Benisty, M., Teague, R., et al. 2019, *ApJ*, 879, L25
- Jäger, C., Molster, F. J., Dorschner, J., et al. 1998, *A&A*, 339, 904
- Jang, H., Waters, L. B. F. M., Kamp, I., & Dullemond, C. P. 2024, *arXiv e-prints*, arXiv:2405.00375
- Jorge, D., Kamp, I., Waters, R., Woitke, P., & Spaargaren, R. 2021, in *European Planetary Science Congress, EPSC2021–853*
- Juhász, A., Bouwman, J., Henning, T., et al. 2010, *ApJ*, 721, 431
- Juhász, A., Henning, T., Bouwman, J., et al. 2009, *ApJ*, 695, 1024
- Kaeufer, T., Min, M., Woitke, P., Kamp, I., & Arabhavi, A. M. 2024, *A&A*, 687, A209
- Kama, M., Min, M., & Dominik, C. 2009, *A&A*, 506, 1199
- Kemper, F., Vriend, W. J., & Tielens, A. G. G. M. 2004, *ApJ*, 609, 826
- Keppler, M., Benisty, M., Müller, A., et al. 2018, *A&A*, 617, A44
- Kessler-Silacci, J., Augereau, J.-C., Dullemond, C. P., et al. 2006, *ApJ*, 639, 275
- Kessler-Silacci, J. E., Hillenbrand, L. A., Blake, G. A., & Meyer, M. R. 2005, *ApJ*, 622, 404
- Koike, C., Chihara, H., Tsuchiyama, A., et al. 2003, *A&A*, 399, 1101
- Lebouteiller, V., Barry, D. J., Spoon, H. W. W., et al. 2011, *ApJS*, 196, 8
- Long, Z. C., Akiyama, E., Sitko, M., et al. 2018, *ApJ*, 858, 112
- Mathis, J. S., Rimpl, W., & Nordsieck, K. H. 1977, *ApJ*, 217, 425
- Mesa, D., Keppler, M., Cantalloube, F., et al. 2019, *A&A*, 632, A25
- Min, M., Hovenier, J. W., & de Koter, A. 2005, *A&A*, 432, 909
- Min, M., Hovenier, J. W., Dominik, C., de Koter, A., & Yurkin, M. A. 2006, *J. Quant. Spectr. Rad. Transf.*, 97, 161
- Min, M., Waters, L. B. F. M., de Koter, A., et al. 2007, *A&A*, 462, 667
- Müller, A., Keppler, M., Henning, T., et al. 2018, *A&A*, 617, L2
- Oliveira, I., Olofsson, J., Pontoppidan, K. M., et al. 2011, *ApJ*, 734, 51
- Olofsson, J., Augereau, J. C., van Dishoeck, E. F., et al. 2010, *A&A*, 520, A39
- Olofsson, J., Juhász, A., Henning, T., et al. 2012, *A&A*, 542, A90
- Perotti, G., Christiaens, V., Henning, T., et al. 2023, *Nature*, 620, 516
- Pinilla, P., Benisty, M., Waters, R., Bae, J., & Facchini, S. 2024, *arXiv e-prints*, arXiv:2403.07057
- Pinilla, P., Klarman, L., Birnstiel, T., et al. 2016, *A&A*, 585, A35
- Portilla-Revelo, B., Kamp, I., Facchini, S., et al. 2023, *A&A*, 677, A76
- Raymond, S. N. & Morbidelli, A. 2022, in *Astrophysics and Space Science Library*, Vol. 466, *Demographics of Exoplanetary Systems*, Lecture Notes of the 3rd Advanced School on Exoplanetary Science, ed. K. Biazzo, V. Bozza, L. Mancini, & A. Sozzetti, 3–82
- Rieke, G. H., Wright, G. S., Böker, T., et al. 2015, *PASP*, 127, 584
- Rigby, J., Perrin, M., McElwain, M., et al. 2023, *PASP*, 135, 048001
- Sargent, B. A., Forrest, W. J., Tayrien, C., et al. 2009, *ApJS*, 182, 477
- Schoonenberg, D. & Ormel, C. W. 2017, *A&A*, 602, A21
- Servino, J. L. & Piriou, B. 1973, *Physica Status Solidi B Basic Research*, 55, 677
- Sicilia-Aguilar, A., Bouwman, J., Juhász, A., et al. 2009, *ApJ*, 701, 1188
- Sturm, B., Bouwman, J., Henning, T., et al. 2013, *A&A*, 553, A5
- Tamanai, A. & Mutschke, H. 2010, *Infrared Spectroscopy of Dust Particles in Aerosols for Astronomical Application*, 101–123
- Tamanai, A., Mutschke, H., & Blum, J. 2009, in *Astronomical Society of the Pacific Conference Series*, Vol. 414, *Cosmic Dust - Near and Far*, ed. T. Henning, E. Grün, & J. Steinacker, 438
- Tamanai, A., Mutschke, H., Blum, J., & Meeus, G. 2006, *ApJ*, 648, L147
- Thanathibodee, T., Calvet, N., Bae, J., Muzerolle, J., & Hernández, R. F. 2019, *ApJ*, 885, 94
- Trotta, R. 2008, *Contemporary Physics*, 49, 71
- van Boekel, R., Min, M., Leinert, C., et al. 2004, *Nature*, 432, 479
- van Boekel, R., Min, M., Waters, L. B. F. M., et al. 2005, *A&A*, 437, 189
- van Boekel, R., Waters, L. B. F. M., Dominik, C., et al. 2003, *A&A*, 400, L21
- Virtanen, P., Gommers, R., Oliphant, T. E., et al. 2020, *Nature Methods*, 17, 261
- Wagner, K., Follete, K. B., Close, L. M., et al. 2018, *ApJ*, 863, L8
- Watson, D., Leisenring, J. M., Furlan, E., et al. 2009, *ApJS*, 180, 84
- Woitke, P., Helling, C., Hunter, G. H., et al. 2018, *A&A*, 614, A1
- Wright, G. S., Rieke, G. H., Glasse, A., et al. 2023, *PASP*, 135, 048003
- Wright, G. S., Wright, D., Goodson, G. B., et al. 2015, *PASP*, 127, 595
- Zhou, Y., Bowler, B. P., Wagner, K. R., et al. 2021, *AJ*, 161, 244

¹ Department of Astrophysics/IMAPP, Radboud University, PO Box 9010, 6500 GL Nijmegen, The Netherlands
e-mail: hyerin.jang@astro.ru.nl

² SRON Netherlands Institute for Space Research, Niels Bohrweg 4, NL-2333 CA Leiden, the Netherlands

³ Space Research Institute, Austrian Academy of Sciences, Schmiedlstrasse 6, 8042 Graz, Austria

⁴ Kapteyn Astronomical Institute, Rijksuniversiteit Groningen, Postbus 800, 9700AV Groningen, The Netherlands

⁵ Institute for Theoretical Physics and Computational Physics, Graz University of Technology, Petersgasse 16, 8010 Graz, Austria

⁶ RIKEN Cluster for Pioneering Research, 2-1 Hirosawa, Wako-shi, Saitama 351-0198, Japan

⁷ Max-Planck-Institut für Astronomie (MPIA), Königstuhl 17, 69117 Heidelberg, Germany

⁸ Institute of Astronomy, KU Leuven, Celestijnenlaan 200D, 3001 Leuven, Belgium

⁹ STAR Institute, Université de Liège, Allée du Six Août 19c, 4000 Liège, Belgium

¹⁰ Centro de Astrobiología (CAB), CSIC-INTA, ESAC Campus, Camino Bajo del Castillo s/n, 28692 Villanueva de la Cañada, Madrid, Spain

¹¹ Leiden Observatory, Leiden University, 2300 RA Leiden, the Netherlands

¹² Max-Planck Institut für Extraterrestrische Physik (MPE), Giessenbachstr. 1, 85748, Garching, Germany

¹³ Dept. of Astrophysics, University of Vienna, Türkenschanzstr. 17, A-1180 Vienna, Austria

- ¹⁴ ETH Zürich, Institute for Particle Physics and Astrophysics,
Wolfgang-Pauli-Str. 27, 8093 Zürich, Switzerland
- ¹⁵ Université Paris-Saclay, Université Paris Cité, CEA, CNRS, AIM,
F-91191 Gif-sur-Yvette, France
- ¹⁶ SRON Netherlands Institute for Space Research, PO Box 800, 9700
AV, Groningen, The Netherlands
- ¹⁷ Université Paris-Saclay, CNRS, Institut d'Astrophysique Spatiale,
91405, Orsay, France

Appendix A: Additional dust retrieval results

In this paper, we show multiple dust fitting models for MIRI spectrum with different sets of dust opacities, dust compositions, and also for Spitzer data. The mass fractions of each dust species and sizes in the models are summarized in Table A.1. The results of Model DHS and Model Aerosol are shown in Fig. A.1 and Fig. A.2, respectively.

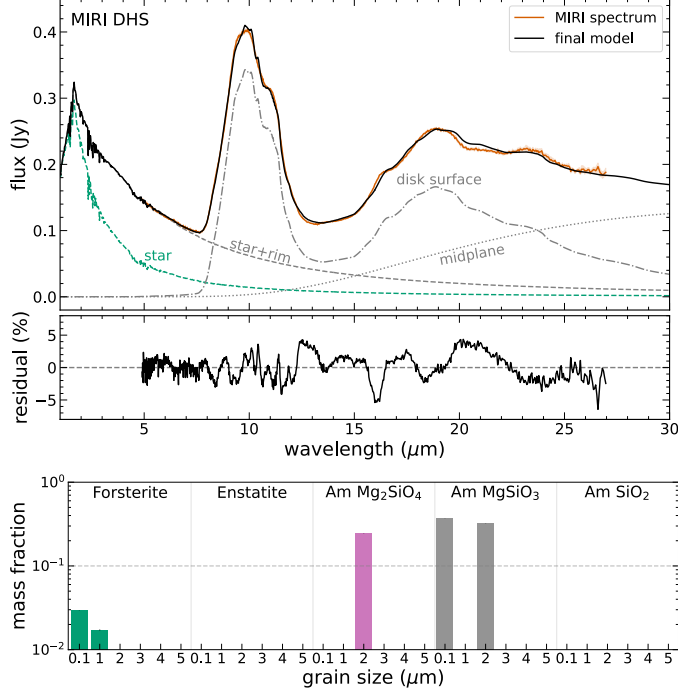


Fig. A.1: Fitting with DHS opacity. The modeled spectrum generally matches well with the MIRI spectrum except the overestimation around $20\ \mu\text{m}$. Amorphous silicates still dominate the dust mass abundance, and enstatite and silica are not detected.

Appendix B: Posterior probability distribution

Figure B.1 is the posterior probability distributions of Model GRF, the best model for MIRI data. The temperatures of each component are derived through Bayesian analysis, while scale factors and dust abundances are estimated using the non-negative square fitting. Circular contours suggest that results are independent from other parameters. In contrast, tilted elliptical contours indicate certain dependency between components. For example, the $0.1\ \mu\text{m}$ -sized amorphous MgSiO_3 and surface temperature exhibit a degeneracy. As the temperature decreases, the abundance increases, which is natural to balance the flux contribution. Although some other degenerate relations do not follow this trend, they vary within very small range, demonstrating that abundances and temperatures are well-constrained.

Appendix C: Shifting the $23\text{--}24\ \mu\text{m}$ band peak

The peak position of $23\text{--}24\ \mu\text{m}$ band does not only depend on the relative fraction of iron with respect to magnesium but also on grain size. As the grain is larger, the peak position shifts to the longer wavelength. For $0.1\ \mu\text{m}$, $2\ \mu\text{m}$, and $3\ \mu\text{m}$, the peak positions shift from $23.27\ \mu\text{m}$ to $23.46\ \mu\text{m}$ and $23.66\ \mu\text{m}$ as shown in Fig. C.1.

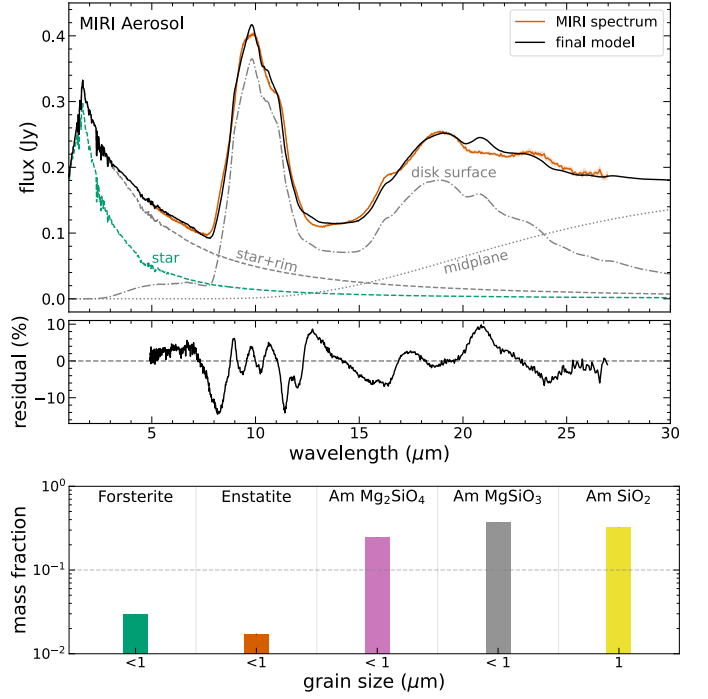


Fig. A.2: Fitting with Aerosol measurements. The shape of the fitted model roughly matches with some mismatches at, for example, $17\ \mu\text{m}$ and $22\ \mu\text{m}$, resulting large residuals. Amorphous silicates still dominate the mass fraction. Unlike from the models with GRF and DHS, enstatite and amorphous SiO_2 appear less than 10 %.

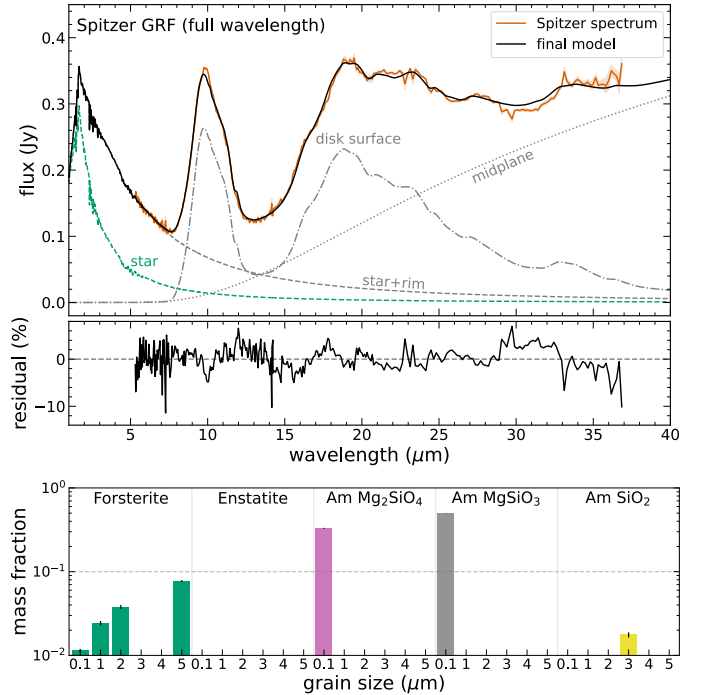


Fig. A.3: Fitting of Spitzer data for full wavelength range ($5\text{--}37\ \mu\text{m}$)

Table A.1: Mass fraction of dust species and their grain sizes for each model. Most of errorbars is less than 0.01 %, and the largest errorbar is still less than 0.2 %. Thus, we do not denote these small errorbars in this table.

name	grain model	species	mass fraction [%]						
			0.1 μm	1 μm	2 μm	3 μm	4 μm	5 μm	total
Model GRF	GRF	Forsterite	0	5.7	2.7	0	0	12.0	20.4
		Enstatite	<1	0	0	0	0	0	<1
		Amorphous Mg ₂ SiO ₄	0	5.8	0	23.4	0	0	29.2
		Amorphous MgSiO ₃	32.8	4.6	0	0	12.4	0	49.8
		Amorphous SiO ₂	0	0	0	0	0	0	0
Model GRF _{4μm}	GRF	Forsterite	0	5.8	1.7	2.0	7.9	-	17.4
		Enstatite	<1	0	0	0	0	0	<1
		Amorphous Mg ₂ SiO ₄	0	5.1	0	25.9	0	0	31.0
		Amorphous MgSiO ₃	33.9	4.5	0	0	1.3	0	39.7
		Amorphous SiO ₂	0	0	0	0	0	0	0
Model GRF _{2μm}	GRF	Forsterite	0	5.0	7.2	-	-	-	12.2
		Enstatite	<1	0	0	0	0	0	<1
		Amorphous Mg ₂ SiO ₄	0	0	19.3	14.7	0	0	34.0
		Amorphous MgSiO ₃	39.2	<1	0	0	13.7	0	52.9
		Amorphous SiO ₂	<1	0	0	0	0	0	<1
Model DHS	DHS	Forsterite	2.9	1.7	0	0	0	0	4.6
		Enstatite	0	0	0	0	0	<1	<1
		Amorphous Mg ₂ SiO ₄	0	0	24.5	0	0	<1	24.5
		Amorphous MgSiO ₃	37.2	0	32.3	0	0	0	69.5
		Amorphous SiO ₂	0	<1	0	0	0	0	<1
Model Aerosol		Forsterite	-	3.2	-	-	-	-	3.2
		Enstatite	-	2.1	-	-	-	-	2.1
		Amorphous Mg ₂ SiO ₄	-	61.2	-	-	-	-	61.2
		Amorphous MgSiO ₃	-	26.0	-	-	-	-	26.0
		Amorphous SiO ₂	-	7.4	-	-	-	-	7.4
Model Mg+Fe	GRF	Forsterite	0	4.7	4.7	0	0	4.5	13.9
		Enstatite	<1	0	0	0	0	0	<1
		Fayalite	<1		0	0	0	0	<1
		Amorphous Mg ₂ SiO ₄	12.9	0	0	0	0	0	12.9
		Amorphous MgFeSiO ₄	0	0	0	0	11.4	9.2	20.6
		Amorphous MgSiO ₃	27.0	8.11	0	0	0	0	35.11
		Amorphous MgFeSi ₂ O ₆	0	0	0	0	0	15.9	15.9
		Amorphous SiO ₂	0	0	0	0	0	0	0
Model Spitzer	GRF	Forsterite	0	3.7	6.1	0	0	0	9.8
		Enstatite	0	0	0	0	0	0	0
		Amorphous Mg ₂ SiO ₄	36.0	0	0	0	0	0	36.0
		Amorphous MgSiO ₃	37.6	12.7	0	0	0	0	50.3
		Amorphous SiO ₂	0	0	0	0	0	3.8	3.8
Model Spitzer(full)	GRF	Forsterite	<1	3.2	2.7	0	0	8.6	14.5
		Enstatite	0	0	0	0	0	0	0
		Amorphous Mg ₂ SiO ₄	33.4	0	0	0	0	0	33.4
		Amorphous MgSiO ₃	49.7	0	0	0	0	0	49.7
		Amorphous SiO ₂	0	0	0	1.6	0	0	1.6

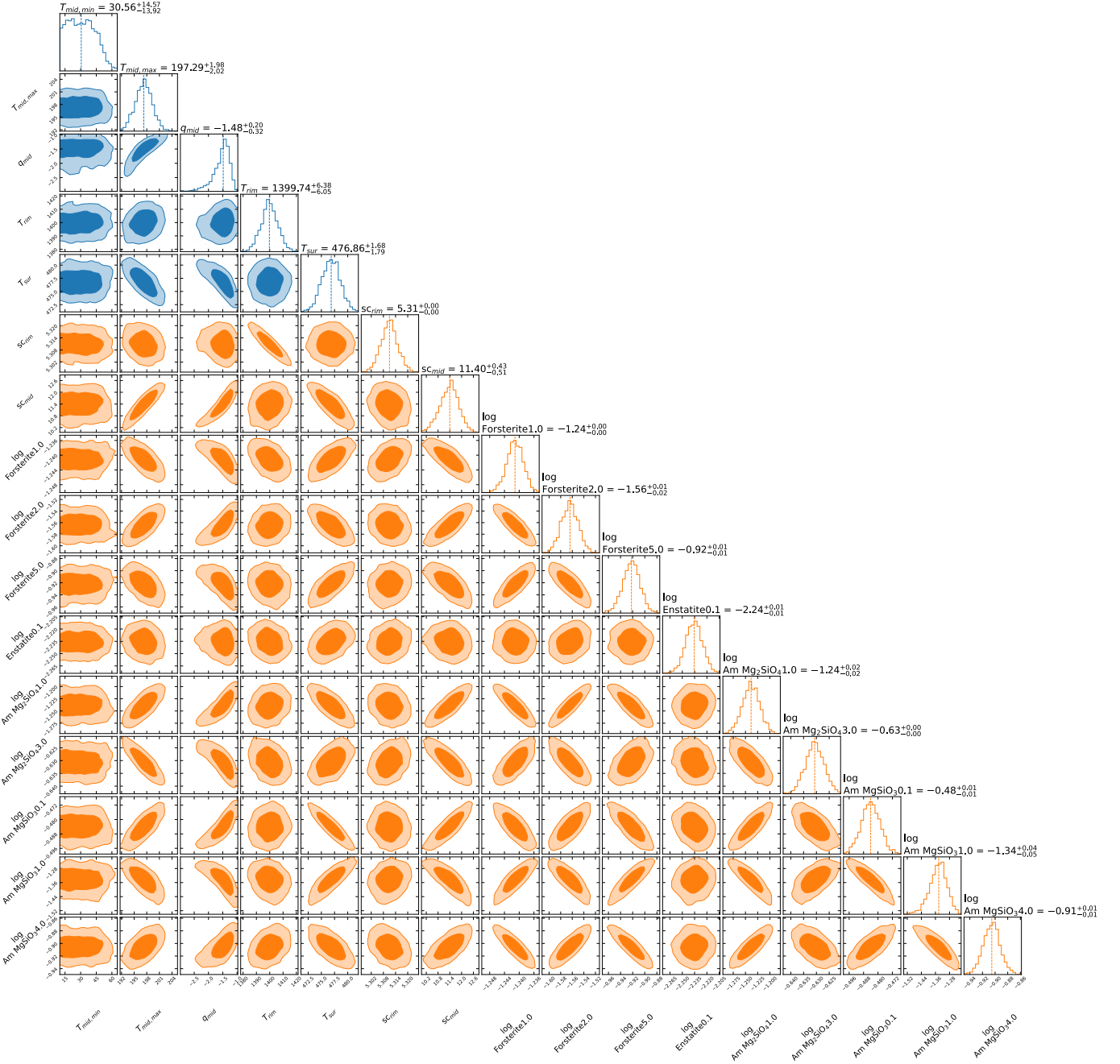


Fig. B.1: Posterior probability distributions of Model GRF. The scale factors for inner rim (sc_{rim}) and midplane (sc_{mid}) components and dust abundances are estimated by the non-negative least square fitting (orange), while the other parameters are determined by Bayesian analysis (blue). The error bars represent the 16th and 84th percentile that correspond to the -1 sigma and 1 sigma uncertainties of the retrieved values.

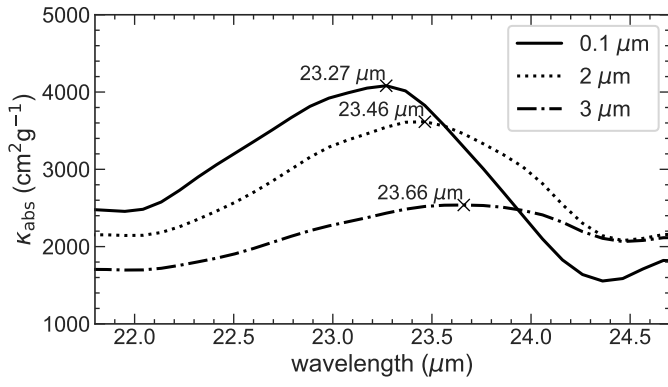


Fig. C.1: 23–24 μm crystalline features of different grain sizes in GRF opacities. As the grain sizes become large, the peak shifts to longer wavelength.